Cell

Resource

Early Alzheimer's disease pathology in human cortex involves transient cell states

Graphical abstract

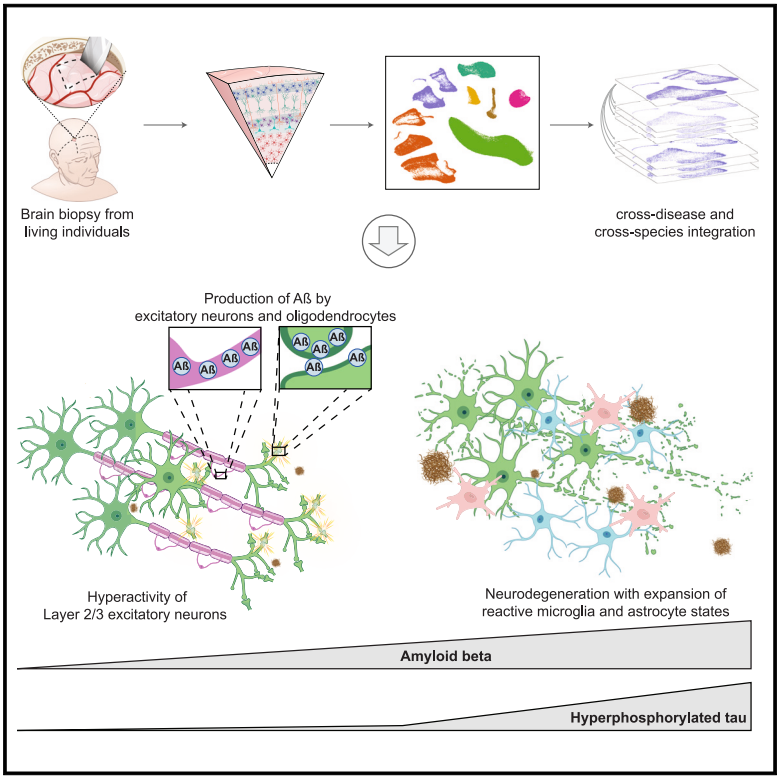

Highlights

- Single-nucleus profiling of human cortex biopsies uncovers amyloid-associated states
- Upper-layer pyramidal neurons show hyperactivity prior to degeneration
- Microglial states correlate with pathological and clinical progression
- Signatures of amyloid production identified in both neurons and oligodendrocytes

Authors

Vahid Gazestani, Tushar Kamath, Naeem M. Nadaf, ..., Beth Stevens, Ville Leinonen, Evan Z. Macosko

Correspondence

emacosko@broadinstitute.org

In brief

Generating single-nucleus atlas from cortical biopsies of living individuals at early stage of Alzheimer's disease, cell states of neurons, microglia, and oligodendrocytes associated with AD pathology are identified.

Gazestani et al., 2023, Cell *186*, 4438–4453
September 28, 2023
https://doi.org/10.1016/j.cell.2023.08.005

CellPress

CellPress

Cell

Resource

Early Alzheimer's disease pathology in human cortex involves transient cell states

Vahid Gazestani,[1,15] Tushar Kamath,[1,2,15] Naeem M. Nadaf,[1] Antonios Dougalis,[3] S.J. Burris,[1] Brendan Rooney,[4] Antti Junkkari,[5,6] Charles Vanderburg,[1] Anssi Pelkonen,[3] Mireia Gomez-Budia,[3] Nelli-Noora Välimäki,[3] Tuomas Rauramaa,[5,7] Martine Therrien,[1] Anne M. Koivisto,[4,5,8,9,10] Matthew Tegtmeyer,[1] Sanna-Kaisa Herukka,[5,8] Abdulraouf Abdulraouf,[1] Samuel E. Marsh,[11] Mikko Hiltunen,[12] Ralda Nehme,[1] Tarja Malm,[3] Beth Stevens,[1,11,13] Ville Leinonen,[5,6] and Evan Z. Macosko[1,14,16,*]

[1]Broad Institute of MIT and Harvard, Cambridge, MA 02142, USA
[2]Harvard Graduate Program in Biophysics and Harvard/MIT MD-PhD Program, Harvard University, Cambridge, MA 02139, USA
[3]A.I. Virtanen Institute for Molecular Sciences, University of Eastern Finland, Kuopio, Finland
[4]Program in Neuroscience, Harvard Medical School, Boston, MA 02115, USA
[5]Institute of Clinical Medicine, University of Eastern Finland, Kuopio, Finland
[6]Department of Neurosurgery, Kuopio University Hospital, Kuopio, Finland
[7]Department of Pathology, Kuopio University Hospital, Kuopio, Finland
[8]Department of Neurology, Kuopio University Hospital, Kuopio, Finland
[9]Department of Neurosciences, University of Helsinki, Helsinki, Finland
[10]Department of Geriatrics, Helsinki University Hospital, Helsinki, Finland
[11]F.M. Kirby Neurobiology Center, Boston Children's Hospital, Boston, MA 02115, USA
[12]Institute of Biomedicine, University of Eastern Finland, Kuopio, Finland
[13]Howard Hughes Medical Institute (HHMI), Boston, MA 02115, USA
[14]Massachusetts General Hospital, Department of Psychiatry, Boston, MA 02114, USA
[15]These authors contributed equally
[16]Lead contact
*Correspondence: emacosko@broadinstitute.org
https://doi.org/10.1016/j.cell.2023.08.005

SUMMARY

Cellular perturbations underlying Alzheimer's disease (AD) are primarily studied in human postmortem samples and model organisms. Here, we generated a single-nucleus atlas from a rare cohort of cortical biopsies from living individuals with varying degrees of AD pathology. We next performed a systematic cross-disease and cross-species integrative analysis to identify a set of cell states that are specific to early AD pathology. These changes—which we refer to as the early cortical amyloid response—were prominent in neurons, wherein we identified a transitional hyperactive state preceding the loss of excitatory neurons, which we confirmed by acute slice physiology on independent biopsy specimens. Microglia overexpressing neuroinflammatory-related processes also expanded as AD pathology increased. Finally, both oligodendrocytes and pyramidal neurons upregulated genes associated with β-amyloid production and processing during this early hyperactive phase. Our integrative analysis provides an organizing framework for targeting circuit dysfunction, neuroinflammation, and amyloid production early in AD pathogenesis.

INTRODUCTION

The first pathological sign of Alzheimer's disease (AD) in the human cortex is the gradual accumulation of β-amyloid plaques, followed by the appearance of gliosis, misfolded tau, and neurodegeneration. Of critical importance is understanding the coordinated activities of neurons and glia during the early phases of the disease that initiate this pathogenic cascade.[1,2] Postmortem single-cell studies have identified disease-associated cellular changes in AD, particularly at later histopathological stages.[3–8] Inference from postmortem samples can be complicated by peri-mortem transcriptional responses to agonal state, cessation of blood flow, hypoxia, and neuronal atrophy. Prior cytological[9–11] and transcriptional[12] analyses demonstrate a marked decline, particularly in neurons, of cell health within 2–4 h postmortem. Consequently, several fundamental questions related to the early stages of AD remain unanswered, including which cell types are perturbed the most, what molecular mechanisms are dysregulated in neuronal types of different cortical layers, and how these early perturbations contribute to the production of misfolded proteins and the progression of pathology in the human brain.

We reasoned that a deep analysis of samples from living individuals harboring various extents of amyloid deposits could

enable the measurement of veridical cell states associated with early-stage pathology. We therefore performed single-nucleus RNA sequencing (snRNA-seq) on a rare set of surgical biopsies from patients undergoing ventriculoperitoneal shunt placement for treatment of suspected normal pressure hydrocephalus (NPH). In a study of 335 individuals, 44% of biopsies contained β-amyloid (Aβ) plaques,[13] and most importantly, longitudinal follow-up of multiple NPH cohorts demonstrated an association between the presence of Aβ within biopsies and a future clinical diagnosis of AD.[13–15] To ensure that our insights were not restricted to a single cohort and were specific to AD, we further developed an accurate integrative analysis framework to incorporate published postmortem and mouse model single-cell datasets to construct a compendium of 2.4 million uniformly annotated cell profiles across diseases and species. The resulting analyses revealed what we collectively term the early cortical amyloid response (ECAR): a suite of consistent tissue changes in specific cell types that co-occur with the initial onset of brain amyloidosis.

RESULTS

A single-nucleus atlas of human brain biopsies to identify AD pathological perturbations

To capture cellular perturbations in the cortex of living individuals in response to AD pathology, we collected biopsies—frozen within 5 min of surgical excision to ensure fidelity of *in vivo* transcriptional states—from the frontal cortices (Brodmann areas 8 and 9) of 52 patients with NPH (Figure 1A). Histopathological examination of the biopsies identified 19 with Aβ plaques (Aβ+), 8 with both Aβ plaques and phosphorylated tau pathology (Aβ+Tau+), and 25 that were free of histopathology (Table S1). From the stereotactic position of the catheter insertion site recorded by post-surgical computed tomography (CT) or MRI, we determined that the anatomical location of sampling did not correlate with AD histopathological burden (Figure S1A). We further divided the Aβ+ biopsies into three groups by their level of plaque burden (Figures S1B and S1C). The amount of Aβ plaques and tau tangles correlated inversely with these patients' Aβ-42 cerebrospinal fluid (CSF) levels (p value < 0.001; Figure 1B) and positively with CSF levels of phosphorylated tau (p value < 0.005; Figure 1B), consistent with prior biomarker studies of AD progression.[16,17] Moreover, the CSF levels of phosphorylated tau in Aβ+ individuals were similar to individuals without histopathology (p value > 0.95; Student's t test) and significantly less than an independent cohort of 36 clinically diagnosed AD individuals (p value < 0.004; Student's t test; Figure 1B). Collectively, these results suggest the severity of biopsy histopathology is representative of the overall burden on the brain.

To more directly establish the relevance of the observed histopathology to the clinical stage of the disease, we compared the clinical cognitive mini-mental state examination (MMSE) scores of individuals with Aβ+ and Aβ+Tau+ biopsies with the control individuals from our cohort. The subjects with Aβ+ biopsies had significantly lower MMSE cognitive scores compared with controls (p value: 0.04; Cohen d: 0.70; Table S1). Moreover, the Aβ+Tau+ individuals had an even stronger cognitive decline relative to the individuals whose biopsies were free of amyloid and tau histopathology (p value: 0.009; Cohen d: 0.97). We further reviewed longitudinal clinical records of the 52 individuals for a median of 5 years after biopsy collection (STAR Methods). A clinical diagnosis of AD was made in all 8 Aβ+Tau+ individuals prior to, or within 1 year of, the time of biopsy. Moreover, 9 of the 19 Aβ+ individuals were also diagnosed with AD in longitudinal follow-ups, representing an incidence rate of 47% and a 4.5-fold odds increase over individuals with amyloid-free biopsies (p value < 0.05). These analyses of clinical data indicate that the Aβ and tau status of these biopsies is a reasonable indicator of the clinical progression of the disease.

To explore the cell-type-specific changes associated with Aβ and tau histopathology in the cortex, we obtained 892,828 high-quality single-nuclei profiles from this biopsy cohort, with a median of 17,082 nuclei per individual. By unsupervised clustering[18] (STAR Methods), we identified the seven major classes of cells in the cortex: excitatory neurons (ExN; 222,449 nuclei), inhibitory neurons (InN; 83,702 nuclei), microglia (Micro; 59,624 nuclei), astrocytes (Astro; 73,487 nuclei), endothelial cells/pericytes (Endo; 22,407 nuclei), oligodendrocytes (Oligo; 396,292 nuclei), and oligodendrocyte progenitor cells (OPCs; 34,867 nuclei) (Figure 1C). To increase our resolution, we repeated our clustering analysis within each class to identify a total of 82 cell types with a median size of 3,586 nuclei per type.

An integrative analysis of biopsy and postmortem brain

Several studies have profiled brain cells under normal and disease conditions using human postmortem or mouse samples. However, a direct comparison of their results has been hampered by differences in sample qualities, dataset sizes, analysis pipelines, and cell-type annotations. We reasoned that the size and quality of our biopsy dataset would be sufficiently analytically powered to conduct a comprehensive integrative analysis of these datasets with highly granular cell-type specificity. We integrated 27 published single-cell/nucleus studies of the brain derived from both human tissue and mouse models (Figure 1C). Human studies included postmortem samples from individuals with AD, Parkinson's disease (PD), multiple sclerosis (MS), and autism spectrum disorder (ASD) (Table S1). Mouse datasets included models of AD and ALS, as well as de-/re-myelination, aging, prenatal, and food deprivation conditions, among others (Table S1). To accurately combine these datasets with our biopsy cohort, we developed an optimized single-cell integration framework that efficiently handled the substantial technical (e.g., sample preparation, sequencing platforms, and depth) and biological (e.g., human vs. mouse) variation that exists among these datasets (STAR Methods). We next implemented a random walk method to transfer cell-type annotations from our biopsy cohort to each of 27 other studies, thereby uniformly annotating a total of 2,406,980 cells with 82 cell-type labels (Figure 1D; Table S2). Comparison across human datasets demonstrated that our biopsy cohort had among the highest number of cells sampled per cell-type and minimal expression of artifactual genes often associated with sample quality[19,20] (Figure S1). We then investigated how agonal states and the postmortem interval (PMI) affected gene

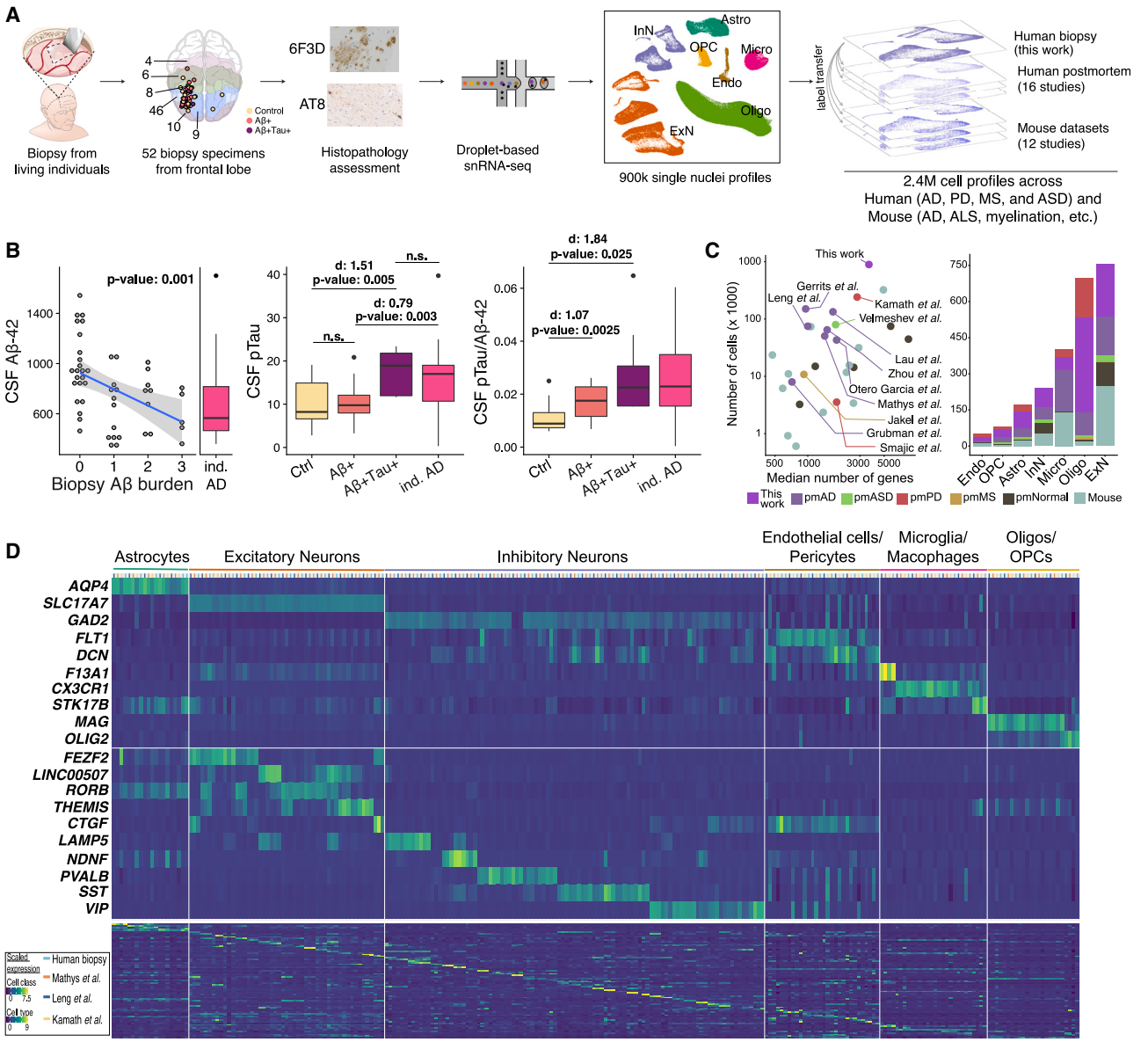

Figure 1. A fresh-tissue atlas of cortical states associated with AD pathology

(A) Schematic of the frontal cortex brain biopsy sampling workflow. Brodmann areas are color-coded in the second panel.

(B) CSF Aβ-42 (left), phosphorylated tau (middle), and ratio of the two (right) in association with Aβ and tau burden scores. The "ind. AD" refers to an independent cohort of 36 NPH patients who were clinically diagnosed with AD prior to, or within 1 year after, CSF collection. Cohen d (d) effect sizes are reported. Left represents the regression line with associated standard error and p value. p values in two right panels are based on student's t test. n.s., not significant.

(C) A summary of datasets that are included in the integrative analysis. pm, postmortem.

(D) Expression of markers of cell classes (top), main neuronal classes (middle), and individual cell types (bottom) across four select human studies. Each row indicates the normalized expression level of each gene across the four human datasets (color-coded on y axis) and 82 cell types. See also Figure S1 and Table S2.

expression patterns in different cell types by comparing our biopsy dataset with postmortem data and identifying recurrent correlates with postmortem interval across datasets. We identified a small but statistically significant decrease in overall gene expression in both excitatory (p value < 0.038; meta-analysis) and inhibitory neurons (p value < 0.024; meta-analysis, Figure S2A), as well as a trend toward increased gene expression in microglia (Figure S2A). Consistently, the ratio of glial-to-neuronal gene expression was lowest in the biopsy dataset and increased with longer postmortem intervals (Figures S2B–S2D). Together, our results, in combination with the expression patterns of artifact-associated genes (Figure S1E), indicate a mild loss of transcriptional complexity in both inhibitory and excitatory neurons, as well as a slight increase in artifact-related genes in microglial cells in response to peri- and postmortem events.

Meta-analysis reveals cortical cellular changes in early AD pathology

To identify cortical tissue changes across the progression of AD pathology, we divided our biopsy samples into those with only Aβ pathology (Aβ+) and those with both Aβ and tau pathologies (Aβ+Tau+). In parallel, we also analyzed two AD postmortem studies[3,4] that sampled both neuronal and glial cells from subjects with low Braak pathology staging and one dataset that only measured glia.[6] We first tested for alterations in relative abundance of cell populations with increasing histopathological burden. A meta-analysis of cell proportions identified two neuron types—NDNF-PROX1 and LINC00507-COL5A2—that were significantly depleted (false discovery rate [FDR]-adjusted p value < 0.05) (Figure 2A) in samples with mild amyloid pathology. The NDNF-PROX1 population expressed *NDNF* and *RELN*, markers of an interneuron type known to reside primarily in layer 1 (L1) of cortex.[21] The LINC00507-COL5A2 population expressed *CUX2* and *LINC00507*, consistent with a layer 2/3 (L2/3) telencephalic identity.[21] Seven additional cell types showed a trend toward significant loss (0.05 < FDR-adjusted p value < 0.12; Table S3): two upper-layer excitatory types (RORB-SCTR, LINC00507-ACVR1C), three inhibitory types (VIP-HTR3A and SST-PENK that are upper-layer-enriched and VIP-NPSR1 that spans cortical layers), one microglia type (CX3CR1), and one oligodendrocyte type (BACE2-L3MBTL4), whereas one microglia type (GPNMB-LPL) showed a trend toward expansion (Figure 2A). We further confirmed that the observed changes in neuronal populations do not correlate with possible confounding factors (Figure S2E). Most importantly, our meta-analysis revealed similar alterations in neuronal and microglial proportions within each of the published postmortem AD case-control cohorts (Figure 2B), underscoring the robustness of the observed cellular changes associated with early-stage AD pathology.

In subjects with high histopathological burden, the proportional losses of the NDNF-PROX1 and LINC00507-COL5A2 neuronal populations were no longer significant (Figures 2A and 2B), likely due to additional loss of other cortical neurons since the overall proportions of excitatory and inhibitory neurons were both lower in these subjects (Figure S2F). Instead, we identified a significant (FDR-adjusted p value < 0.05) expansion of the GPNMB-LPL microglia type and loss of the major homeostatic (HM) microglia population (Figures 2A and 2B). In addition, although not consistently altered in all three human studies (meta-analysis p value < 0.11), one astrocyte population expressing *CHI3L1* and *GFAP* increased in abundance in the late stages of disease in our biopsy cohort (p value < 0.05; odds ratio [OR]): 1.5), one postmortem cohort[4] (p value < 0.075; OR: 1.6), and in a mouse model of AD[22] (p value < 0.02; OR: 1.4) (Table S3). Together, these results indicate that gliosis becomes an increasingly prominent feature of cortical tissue as histopathology worsens.

Next, we examined how the transcriptional phenotype of each cell type changed across the early and late histopathological stages of AD. We implemented a pseudocell-based strategy, coupled with mixed-effect modeling and jack-knifing, to robustly identify differentially expressed (DE) genes in both the Aβ+ and the Aβ+Tau+ biopsies (Figure 2C; Table S4). To better understand the association of gene perturbations with the progression of AD pathology, we compared the transcriptional alterations across cell types in early- and late-stage samples. For most cell types and most notably in microglia populations, we found that the transcriptional alterations quantified in Aβ+Tau+ biopsies were consistent with, but stronger than, those changes measured in Aβ+ samples (Figure 2D). However, several ExN populations showed transcriptional perturbations in the Aβ+ samples that were absent in the Aβ+Tau+ biopsies (Figures 2C and 2D), indicating their passage through a distinct transcriptional state early in histopathological progression. To further assess the extent of overlap in dysregulated transcriptional programs among related cell populations, we calculated the fraction of DE genes in each of the seven major cell classes that show consistent DE within each of their constituent cell types. This comparison demonstrated that DE genes in each of the seven major cell classes exhibited highly preserved perturbation patterns (i.e., similar up- or downregulation patterns) within their related cell types (Figure 2E). Collectively, our DE analyses demonstrated (1) that perturbation of the transcriptomes increases in magnitude as neuropathology worsens, with the exception of ExN s, which show a distinct early phase response, and (2) that individual cell-type responses are largely similar within a major cell class.

Neuronal loss and hyperactivity in early AD pathology

The strongest proportional change in our meta-analysis of the early AD pathological stage was the loss of NDNF-PROX1 InNs (Figure 2A). We therefore wondered whether the loss of these InNs could contribute to the onset and early progression of AD by inducing specific transcriptional states in other cortical cell types. To examine this, we correlated the fraction of NDNF-PROX1 neurons with the extent of molecular perturbations in all other cell types (STAR Methods). Applying this analysis to the Aβ+ biopsy samples identified a specific and significant (FDR-adjusted p value < 0.01) correlation between NDNF-PROX1 depletion and upregulated ExN DE genes in the LINC00507-COL5A2 ExNs (Figures 3A and S3A), which themselves are vulnerable to loss in early AD pathology (Figure 2A). Alternative analysis methods confirmed the strength of association between the ExN DE signature in LINC00507-COL5A2 and the loss of *NDNF*+ expressing cells in Aβ+ individuals (Figures S3B–S3E). Moreover, this association was also significant (FDR-adjusted p value < 0.05) within the control biopsy samples (Figures S3F and S3G), reinforcing that this pair of neuronal changes—loss of NDNF-PROX1 and induction of a specific transcriptional state in LINC00507-COL5A2—occur early in disease. Importantly, the relationship between the InN loss and ExN transcriptional state was specific to NDNF-PROX1 and VIP-HTR3A InNs in Aβ+ biopsies (Figure 3B), the two most depleted inhibitory cell types in the early stage of AD, and was not associated with the loss of other inhibitory populations.

We next sought to better understand the association of the ExN DE signature with Aβ plaque pathology. Comparison of ExN DE genes between Aβ+ and Aβ+Tau+ biopsies revealed a bimodal pattern among upregulated DE genes (Figure 3C), in which one DE gene set was evident solely in the early stage of pathology, whereas another was present in both early- and

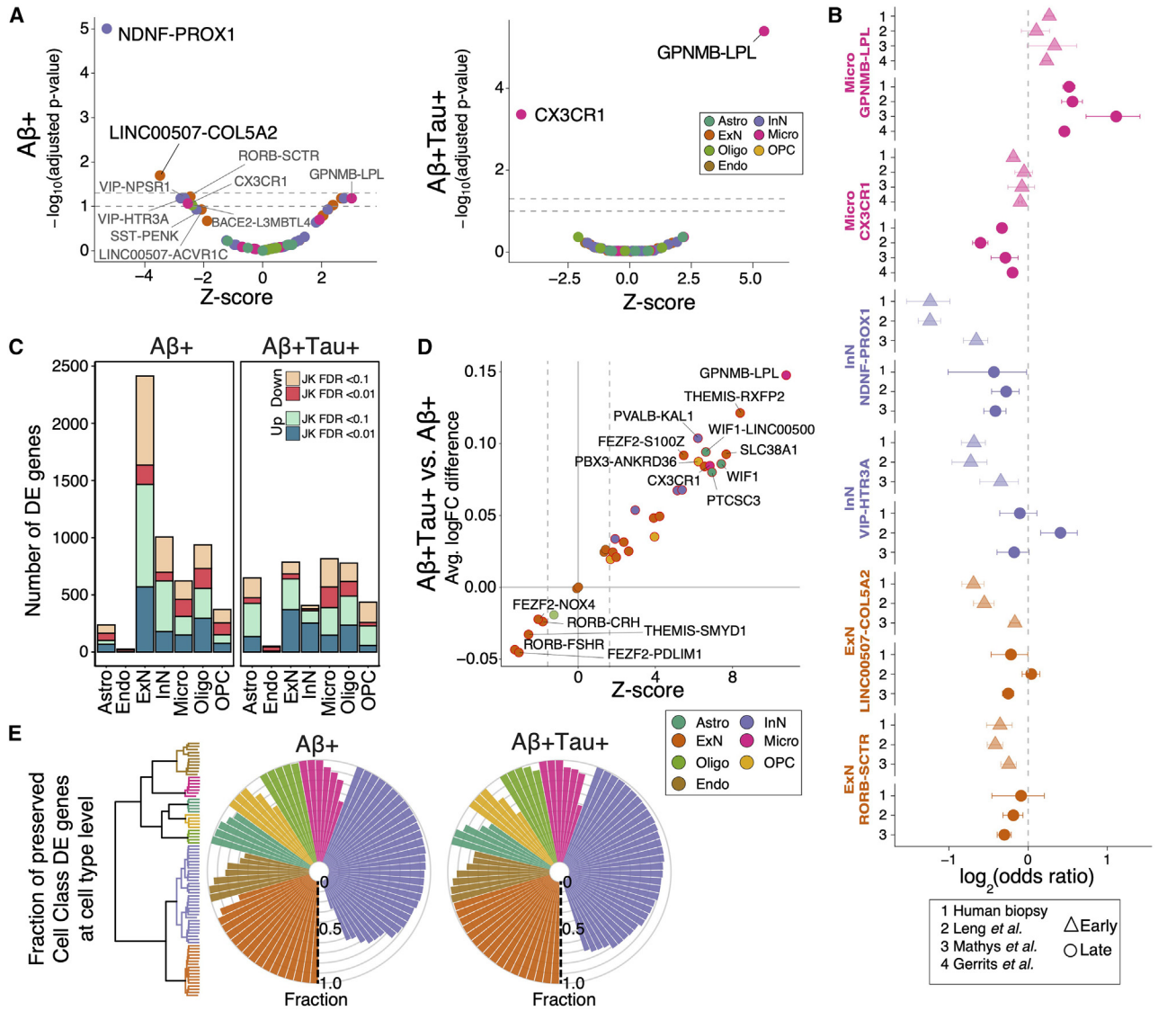

Figure 2. Identification of early- and late-stage cellular perturbations in AD

(A) Volcano plot of a meta-analysis of cell-type proportional changes in early- and late-stage AD-related samples. Colors indicate cell class assignment. Dashed lines represent FDR thresholds of 0.05 and 0.1.

(B) Individual log-odds ratios of six significant cell types in Aβ+ (triangles) and Aβ+Tau+ samples (circles). Whiskers indicate standard errors.

(C) Number of DE genes in each cell class, stratified by biopsy histopathology. JK, jack-knife.

(D) Fold-change concordance of DE genes between Aβ+ and Aβ+Tau+ samples. The y axis shows the average log fold-change (logFC) difference between Aβ+Tau+ and Aβ+. The *Z* scores on the x axis are transformations of p values from a paired t test analysis.

(E) Fraction of DE genes in Aβ+ and Aβ+Tau+ biopsies that are similarly up- or downregulated between the seven major cell classes and their associated subtypes in biopsy samples (based on top 300 protein-coding DE genes at the cell class). The dendrogram illustrates the subdivision of the seven major cell classes into a total of 82 subtypes. See also Figure S2G.

late-stage samples. Given their differences in expression trajectory during AD pathological progression, we asked whether these two sets of DE genes were differentially correlated with NDNF-PROX1 inhibitory loss. Only the DE genes specifically found in response to early AD pathology, particularly within the LINC00507-COL5A2 population, correlated with NDNF-PROX1 proportional loss (Figure 3D).

The activity of L1 *NDNF*-expressing InNs plays a crucial role in the integration of long-range inputs into cortex, particularly through gain modulation of whole cortical columns.[24,25] We wondered if their loss might alter the excitability of nearby L2/3 pyramidal cells. Indeed, we identified a significant association between NDNF-PROX1 loss and upregulation of neural activity response genes[23] specifically within LINC00507-COL5A2 ExNs in Aβ+ individuals (FDR-adjusted p value < 0.01; Figure 3E). Furthermore, Aβ+ biopsy samples with a greater proportional loss of NDNF-PROX1 cells showed a higher percentage of LINC00507-COL5A2 cells expressing canonical activity-regulated

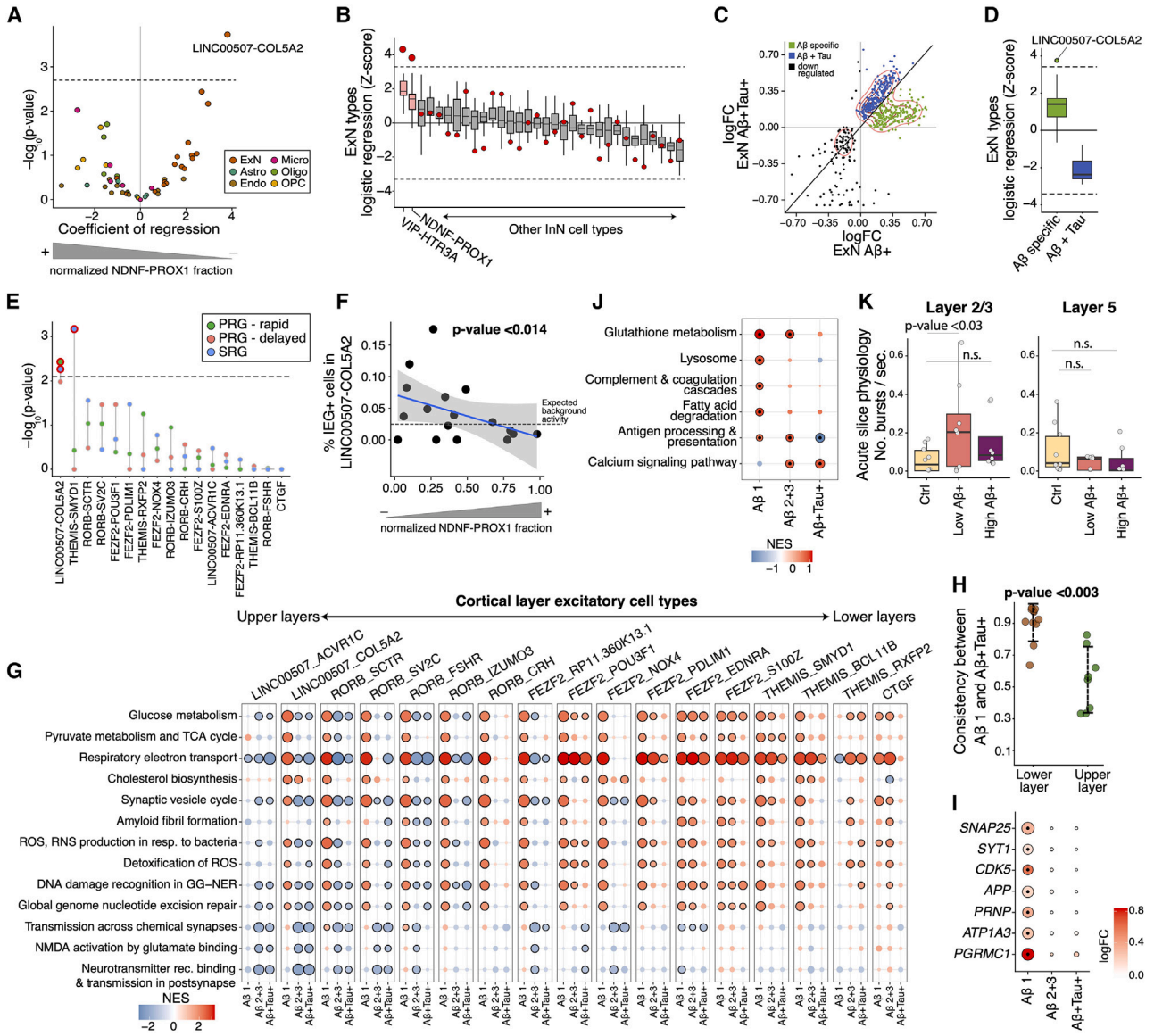

Figure 3. NDNF-PROX1 inhibitory neuron loss is associated with a hyperactivity signature in L2/3 excitatory neurons

(A) Logistic mixed-effect model regression of NDNF-PROX1 proportion versus cell-type transcriptional signature in Aβ+ subjects. The dashed horizontal line represents the FDR threshold of 0.05.

(B) Associations (by logistic mixed-effect model) between the proportion of each inhibitory neuron type with each excitatory type's transcriptional signature in Aβ+ subjects. The red dots indicate the LINC00507-COL5A2 ExNs. See also Figure S3H.

(C) Scatterplot comparing the Aβ+ and Aβ+Tau+ logFC in the ExNs (union of top 300 protein-coding DE genes based on jack-knifed p value).

(D) Logistic mixed-effect model regression of NDNF-PROX1 proportion versus early-specific upregulated DE genes (green dots in C) and upregulated DE genes shared in both Aβ+ and Aβ+Tau+ samples (blue dots in C) for each ExN cell type.

(E) Logistic mixed-effect model regression of NDNF-PROX1 cell fraction versus expression of neural activity signatures[23] in each ExN type in Aβ+ samples (one-sided). PRGs, primary response genes; SRGs, secondary response genes.

(F) Scatterplot showing normalized NDNF-PROX1 fraction (x axis) and the percent of LINC00507-COL5A2 ExNs with high expression of core immediate early genes (y axis, STAR Methods) in Aβ+ subjects. Linear regression line and associated standard error range are represented. A logistic mixed-effect model was used to calculate the p value.

(G) GSEA of Reactome pathways on DE results across ExN types. Dots outlined in black denote significant terms (FDR-adjusted p value < 0.05).

(H) Concordance of DE genes between different stages of AD pathology within excitatory neuron cell types (Student's t test). The *LINC00507+* and *RORB+* were selected as upper-layer excitatory neurons and *FEZF2+*, *CTGF+*, and *THEMIS+* populations as lower layer.

(I) Representation of select ExN DE genes. The outlined dots represent DE genes with jack-knifed FDR-adjusted p value < 0.01.

(J) GSEA of human Kyoto Encyclopedia of Genes and Genomes (KEGG) pathways on *WIF1+* homeostatic astrocytes. Outlined dots represent significant terms (FDR-adjusted p value < 0.1).

(legend continued on next page)

genes[26] (*FOS*, *JUNB*, *ARC*, *NPAS4*, *ERG1*, and *ERG2*; p value < 0.014; Figure 3F). Increased activity of ExNs would be expected to alter their metabolism. Consistent with this, gene set enrichment analysis (GSEA) demonstrated increased expression of metabolism- and mitochondria-related gene sets specifically in biopsies with the lowest level of Aβ plaque burden, further reinforcing the relevance of the hyperactivity phenotype to the early stages of AD pathology (Figure 3G). The enrichment of these terms was diminished in biopsies with higher AD pathological burden (Figure 3G), a pattern that was stronger in upper-layer ExNs. Congruently, comparing samples with the lowest Aβ burden with Aβ+Tau+ demonstrated a significantly higher divergence of the DE patterns of upper-layer neurons compared with the lower layer ExNs (p value < 0.003; Student's t test; Figure 3I). Collectively, our results demonstrate that NDNF-PROX1 InN loss is correlated with hyperactivity and preferential loss of L2/3 ExNs in the prefrontal cortex with low Aβ plaque burden.

Hyperactivity of neurons can perturb pre- and post-synaptic mechanisms.[27] In ExNs from subjects with low Aβ burden, we identified upregulation of *SNAP25*, *SYT1*, and *CDK5*, which are involved in presynaptic vesicle release[28–30] (Figures 3G and 3I). Increased activity of the presynaptic vesicle cycle can elevate Aβ production.[31] Congruently, we found upregulation of genes encoding for protein components involved in Aβ fibril formation, such as *APP* itself, only in the Aβ-low disease samples (Figures 3G and 3I). The oligomeric Aβ receptor genes *PRNP*, *ATP1A3*, and *PGRMC1*, whose protein products influence neuronal activity and synapse functioning through the modulation of N-methyl-D-aspartate (NMDA) receptors[32] and neuronal calcium signaling,[33] were similarly upregulated in ExNs at the early stages of AD pathology (Figure 3I). HM astrocytes also play critical roles in supporting synaptic function and coordinating antioxidant responses, especially in the context of neuronal hyperactivity.[34,35] In our integrative analysis of astrocytes, we identified one *WIF1*+ type with low expression of *GFAP* and high expression of *EAAT1*, *EAAT2*, and *GSTP1* genes, which encode for critical components of glutamate/glutathione cycling (Figures S3I and S3J). The *WIF1*-expressing astrocytes showed enrichment of DE genes related to glutathione metabolism, lysosomal machinery, and fatty acid degradation specifically in subjects with low Aβ burden (Figure 3J), consistent with gene sets previously reported to be upregulated in the astrocytic response to hyperactive neurons.[35] Together, these results suggest that aberrant activity and metabolism of upper-layer pyramidal cells perturb synapse homeostasis and astrocyte functioning in the brain.

Through multiple lines of evidence, we identified hyperactivity of the upper-layer pyramidal neurons in biopsy samples with low Aβ burden that is associated with a selective loss of upper-layer inhibitory and excitatory neurons. To confirm these patterns and establish their functional relevance to AD pathological course, we conducted electrophysiological experiments on acute slices from frontal cortex biopsy samples of an independent cohort of 26 living individuals, including eight samples with low levels of Aβ, eight samples with a high burden of Aβ, and 10 Aβ-free control samples. To assess hyperactivity, baseline neuronal activity was induced in control and Aβ+ samples through treatment with NMDA (Figure S4). In addition to L2/3 pyramidal neurons, we also measured spike activity levels in L5 ExNs as a negative control. Consistent with our results from the analysis of single-nucleus transcriptome data, we observed higher bursting activity in upper-layer ExNs from samples with low Aβ burden (Figure 3K). In contrast, L5 ExNs exhibited similar activities between Aβ+ and control samples (Figure 3K). These findings provide direct functional evidence of hyperactivity of L2/3 ExNs in the human brain at the early stages of AD pathology.

Expanded microglia populations with AD-specific alterations

Our integrative analysis across four AD-related cohorts indicated a mild expansion of *GPNMB*-expressing microglia at early stages of AD pathology that further expanded in samples with higher histopathological burden (Figure 2A). Human genetics and transcriptome studies have implicated microglia in the AD pathogenic process.[36–39] A reactive population expressing *GPNMB* was also identified as enriched in an AD animal model near amyloid plaques,[40] but its connection to human *in vivo* microglial states—in AD, normal aging, and other diseases—remains debated. To more deeply explore microglial states in AD pathology, we leveraged our well-powered integrative analysis of 400,743 microglia profiles across human and mouse studies from diverse brain regions and biological conditions, including 59,624 high-quality microglia nuclei (median number of genes per nucleus = 2,384) from our biopsy cohort. We more deeply sub-clustered the microglia profiles into a total of 13 microglial states (Figures 4A and 4B), including five HM states, a chemokine-enriched state (CRM-CCL3), three reactive states expressing *GPNMB* (GPNMB-NACA, LPL-CD83, and GPNMB-EYA2), an interferon gene-enriched state (IRM-IFIT2), and a proliferative (Prolif) state (Figures 4A and 4B; Table S2). Comparing the microglia populations, we observed the downregulation of microglial markers such as *CX3CR1* and *CSF1R* in the three *GPNMB*-expressing populations relative to the HM microglial cells (Figure 4A). Markers of microglia states correlated strongly across different human brain regions, which is consistent with previous reports[41,42] (Figures S5A–S5D).

Differential expression analysis across all microglia in our cohort identified a pattern that was highly similar in each of the 13 states (Figure S5E), suggesting that all microglia states respond similarly to Aβ accumulation. This transcriptional pattern was also highly consistent across postmortem cohorts and increased in magnitude with further clinical progression of AD (Figures S5F–S5H). The DE signature showed upregulation of genes involved in phagocytosis (*COLEC12*), antigen

(K) Acute slice physiology experiment on biopsy specimens from an independent cohort of 26 individuals. Boxplots quantifying the number of bursts per second in acute slices treated with NMDA from control subjects (Ctrl, n = 10), subjects with low Aβ burden (n = 8), and with high Aβ burden (n = 8). Each dot represents mean spike activity of electrodes for each individual. The p value was computed by a regression analysis with age as a covariate. In all panels with boxplots, Center line, median; box limits, upper and lower quartiles; whiskers, 1.5× interquartile range. See also Figure S4. In (B), (D), and (E), the dashed lines indicate FDR threshold of 0.05.

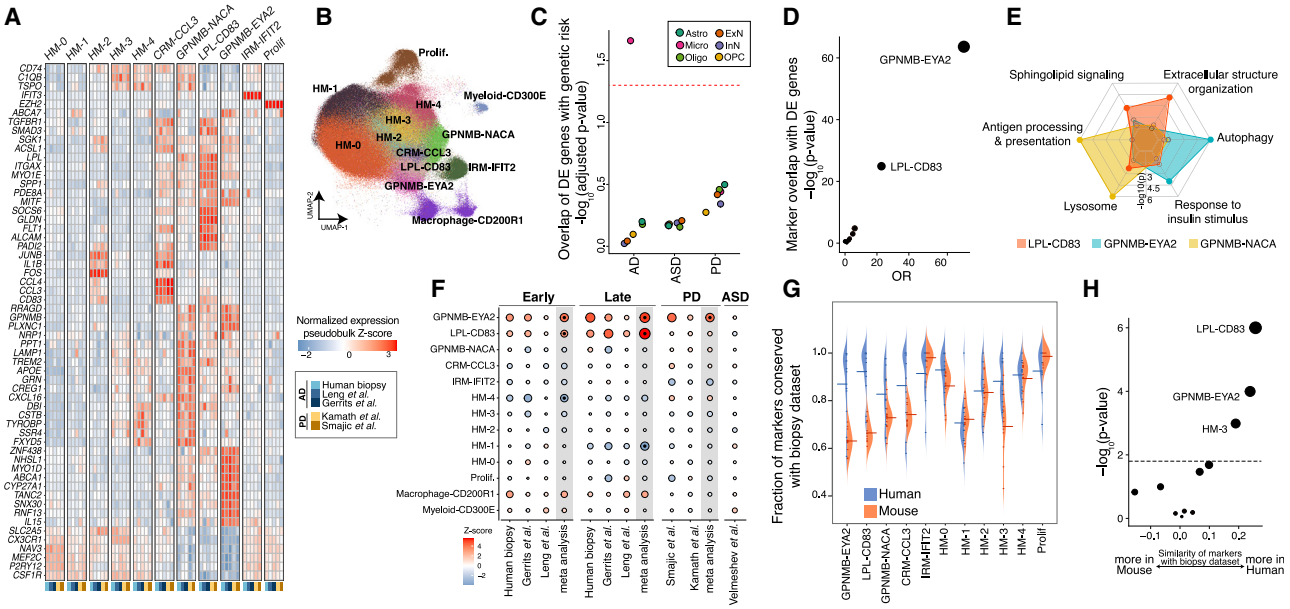

Figure 4. Precise molecular definitions of microglial states activated in early and late AD

(A) Normalized pseudobulk expression of select microglia marker genes across human datasets.

(B) Representation of 13 microglia states.

(C) Dot plot of p values from MAGMA (Multi-marker Analysis of GenoMic Annotation) enrichment analysis[43] of AD, PD, or ASD genetic risk in the upregulated DE genes of each cell class. Dashed line represents an FDR threshold of 0.05.

(D) Dot plot of p values for a Fisher's exact test assessing the overlap between microglial DE genes with top 100 markers of each of the 13 microglial states.

(E) Radar plot representation of enriched gene sets in differential markers of the three GPNMB-LPL microglial states.

(F) Association of proportion of each microglial state with early and late AD pathology, as well as PD and ASD. In meta-analysis columns, black dots represent microglia states with FDR-adjusted p value < 0.05. Points are scaled by the absolute *Z* scores.

(G) Fraction of markers shared between the biopsy cohort and each other dataset (y axis), in each microglial state (x axis). Datasets are stratified by species. Mean values are denoted with a line.

(H) Statistical comparison of the differences in (G) by Student's t test. The dashed line represents an FDR threshold of 0.05.

See also Figure S5.

presentation (*CD74* and members of *HLA* family), lipoprotein metabolism and biosynthesis (*APOE*, *OLR1*, and *ATG7*), fatty acid metabolism (*ACSL1*), autophagy (*ATG7* and *ATG16L2*), and lysosomal function (*ASAH1*, *NPC2*, *SLC11A1*, and *PSAP*) (Table S4). Underscoring the pathological relevance of this common microglial DE signature, we found that it was significantly (FDR-adjusted p value < 0.05) enriched for the expression of genes implicated in AD by common variant case-control studies,[36,37] including *APOE*, *MS4A6A/4A*, *TREM2*, and *INPP5D* (Figure 4C; STAR Methods). In addition, intersection of this DE signature with marker genes for each of the 13 states showed highly significant overlap with markers of GPNMB-EYA2 and LPL-CD83 microglia (FDR-adjusted p value < 0.001; Fisher's exact test; Figure 4D), indicating a transcriptional transition across all microglia cells toward a state resembling the GPNMB-EYA2 and LPL-CD83 populations.

We focused particularly on the three reactive *GPNMB+* states, given their disease relevance. All three states highly expressed genes related to microglial reactivity, including *APOE*, *ITGAX*, *MITF*, and *SGK1* (Figure 4A). However, comparative marker analysis between the three states revealed substantial differences. The GPNMB-NACA population preferentially expressed genes involved in antigen processing and presentation, as well as lysosomal and phagosomal function, relative to the other two states (Figure 4E). By contrast, the GPNMB-EYA2 microglia preferentially expressed genes involved in autophagy (e.g., *IGF1R*, *ATG7*, and *ATG16L2*) and response to insulin (e.g., *MYO5A*, *IGF1R*, and *PPARG*) (Figure 4E). This cell state also expressed interleukin (IL)-15, a key modulator of the nervous system inflammatory response[44] (Figure 4A). The LPL-CD83 microglia expressed genes, including *TGFBR1* and *SMAD3*, which encode for key proteins in transforming growth factor (TGF)-β signaling (Figure 4A), and showed enrichment of genes involved in extracellular structure organization, response to cytokines, focal adhesion, and actin cytoskeleton (Figure 4E). Both IL15 and TGF-β also mediate neuroinflammatory cross-talk between astrocytes and microglia.[45,46] Supporting this notion, we found a strong positive correlation between the expression of *GFAP* in astrocytes and the expansion of GPNMB-EYA2 and LPL-CD83 microglia states in our cohort (Figure S5I). Together, we find transcriptional heterogeneity among reactive microglia cells in human brains that points to specialized functional roles in responding to cues from their surrounding microenvironment.

We next conducted a meta-analysis to ask which of these microglial states is specifically enriched in AD and how these states relate to those found in other neurodegenerative diseases and

disease models. Across the three AD-related datasets with sufficient numbers of microglia to power proportional testing, we identified an expansion of the LPL-CD83 and GPNMB-EYA2 states in both early and late stages of AD histopathology (FDR-adjusted p value < 0.05; Figure 4F). Interestingly, the GPMNB-EYA2 state was also enriched in a meta-analysis of two PD datasets (FDR-adjusted p value < 0.002; Figure 4F), whereas LPL-CD83 was exclusively expanded across the AD datasets. Neither *GPNMB*-expressing microglia population was expanded in individuals with ASD, underscoring the specific role of these microglia in neurodegenerative diseases. In contrast to the human datasets, only the GPNMB-NACA state was consistently expanded in AD mouse models (Figure S5J). This state was also increased in several other mouse datasets, including a model of amyotrophic lateral sclerosis, in both juvenile and aged mice, and in response to demyelinating injury (Figure S5J). To better understand the underlying factors contributing to this apparent divergence in microglia response, we performed a systematic marker analysis of the 13 microglia states across the human and mouse datasets that are included in our integrative analysis. As expected, we found that microglia states are highly consistent across human datasets. Although human microglia states were less preserved in the mouse datasets overall, preservation was notably lower for the mouse LPL-CD83 and GPNMB-EYA2 states (Figures 4G and 4H), suggesting that these transcriptional states are less well recapitulated by laboratory mice. Corroborating this finding, we observed that the *cis*-regulatory regions of marker genes for GPNMB-EYA2 and LPL-CD83 populations are significantly enriched in human-accelerated regions (HARs),[47] fast-evolving regions of the human genome that modulate human-specific transcriptional regulatory programs (Figure S5K). Collectively, our results demonstrate shared and AD-specific microglia responses to disease in the human brain and selective divergence of the most disease-relevant states in mouse models.

Amyloidogenic cell populations in human frontal cortex

The production of amyloid in the brain has largely been assumed to be only in neurons but has been challenging to directly study in human tissue. We leveraged our high-quality surgical biopsy dataset to assess amyloidogenicity in each cell type using transcriptional signatures as a proxy. We took an unbiased approach, assessing the enrichment of a set of 45 genes known to regulate Aβ production and secretion in each cell type (Table S5). Interestingly, GSEA against an ordered list of DE genes for each of the seven cell classes identified not only ExNs but also oligodendrocytes as having significant, positive enrichment for the amyloid gene set (FDR-adjusted p value < 0.05, Figure 5A). The enrichment in these two cell classes was robust to the statistic used to order genes (Figure S6A). A leading-edge analysis identified specific genes that were highly upregulated (including *APP*, *LRRTM3*, and *ITM2B*) and downregulated (such as *BACE2*, *SORL1*, and *PICALM*) in Aβ+ biopsy samples (Figure S6B).

The unexpected enrichment of amyloid-related genes in oligodendrocytes prompted us to investigate whether they share a common DE gene signature with ExNs. Indeed, ExN DE genes overlapped most with those of oligodendrocytes (FDR-adjusted p value < 0.05; Figures 5B and S6C), despite oligodendrocytes sharing the greatest gene expression identity with OPCs (Figure S6D). A gene ontology analysis of the intersecting co-regulated genes identified enrichment of amyloid fibril formation (Figure 5C), further suggesting a similar, shared Aβ-related response. This signature was most prominent in the samples with lowest Aβ burden for both ExNs and oligodendrocytes (FDR-adjusted p value < 0.05, Figures 5D, S6E, and S6F). Leading-edge analysis revealed DE genes involved in multiple aspects of amyloid processing, including downregulation of genes known to either decrease Aβ peptide production or increase clearance, such as *SORL1*, *BACE2*, and *PICALM.* We also detected upregulation of genes involved in amyloid formation, including *RAB11A*, *LRRTM3*, and *APP* itself (Figures 5E and 5F). Crucially, the Aβ gene set was enriched across oligodendrocytes in a meta-analysis of postmortem cohorts with low AD histopathology[3,4] (Figure S6G), but not in DE genes from other disease states, including PD,[49,50] ASD,[51] and MS[52] (Figure 5G), reinforcing its robust and specific association with AD across cohorts.

To experimentally assess the relative Aβ-forming potential of these two cell populations, we differentiated the H1 embryonic stem cell (ESC) line into oligodendrocytes (iOligos) and ExNs (iExNs) (Figure 6A). Single-cell analysis (Figure 6B) of our iOligo cultures showed robust expression of numerous genes known to play roles in myelin function, such as *MBP*, *PLP1*, and *CNP*, as well as transcription factors important for oligodendrocyte differentiation and maturation, such as *SOX10* and *NKX2-2* (Figures 6C and S7D–S7F). These genes were not expressed at high levels in iExNs, which instead expressed canonical neuronal marker genes like *RBFOX3*, *SLC17A7*, and *TUBB3* (Figures 6C and S7A–S7C). Importantly, both cultures expressed appreciable levels of all the necessary machinery to produce β-amyloid protein (Figure 6D). Furthermore, immunohistochemistry of key proteins defining the oligodendrocyte lineage, such as *MBP* and *O4*, showed a linear, significant increase upon induction of *SOX10* (Figures 6E and S7I, p value < 0.05, linear mixed-effect model), whereas markers of other cell types were not significantly associated (Figures S7G and S7H). An ELISA-based quantification of Aβ peptides in iOligos showed a 3-fold increase in Aβ upon *SOX10* induction (Figure 6F), similar to the increase observed upon iExN induction (Figure 6F). Indeed, the total abundance of Aβ—when corrected for the total number of mature cells in the culture—was not significantly different (p = 0.497, Student's t test, Figure 6F) between iExNs and iOligos at their respective differentiation endpoints, suggesting a similar intrinsic capacity to produce Aβ. As predicted by our transcriptional analyses, we could not detect any Aβ in media taken from ESC-derived microglia cultures (Figure S7J). Furthermore, treatment of both iOligos and iExNs with beta-secretase (BACE) or gamma-secretase inhibitors caused a 10-fold reduction in total Aβ protein levels in both cell types (Figure 6G). Finally, we sought to determine whether the species composition of amyloid peptide production was significantly different between cell types given the well-established higher aggregation and amyloid formation potential of longer species. We found that Aβ species ratios were not significantly different (p value = 0.64, Student's t test, Figure 6H) between iOligos and iExNs, suggesting that

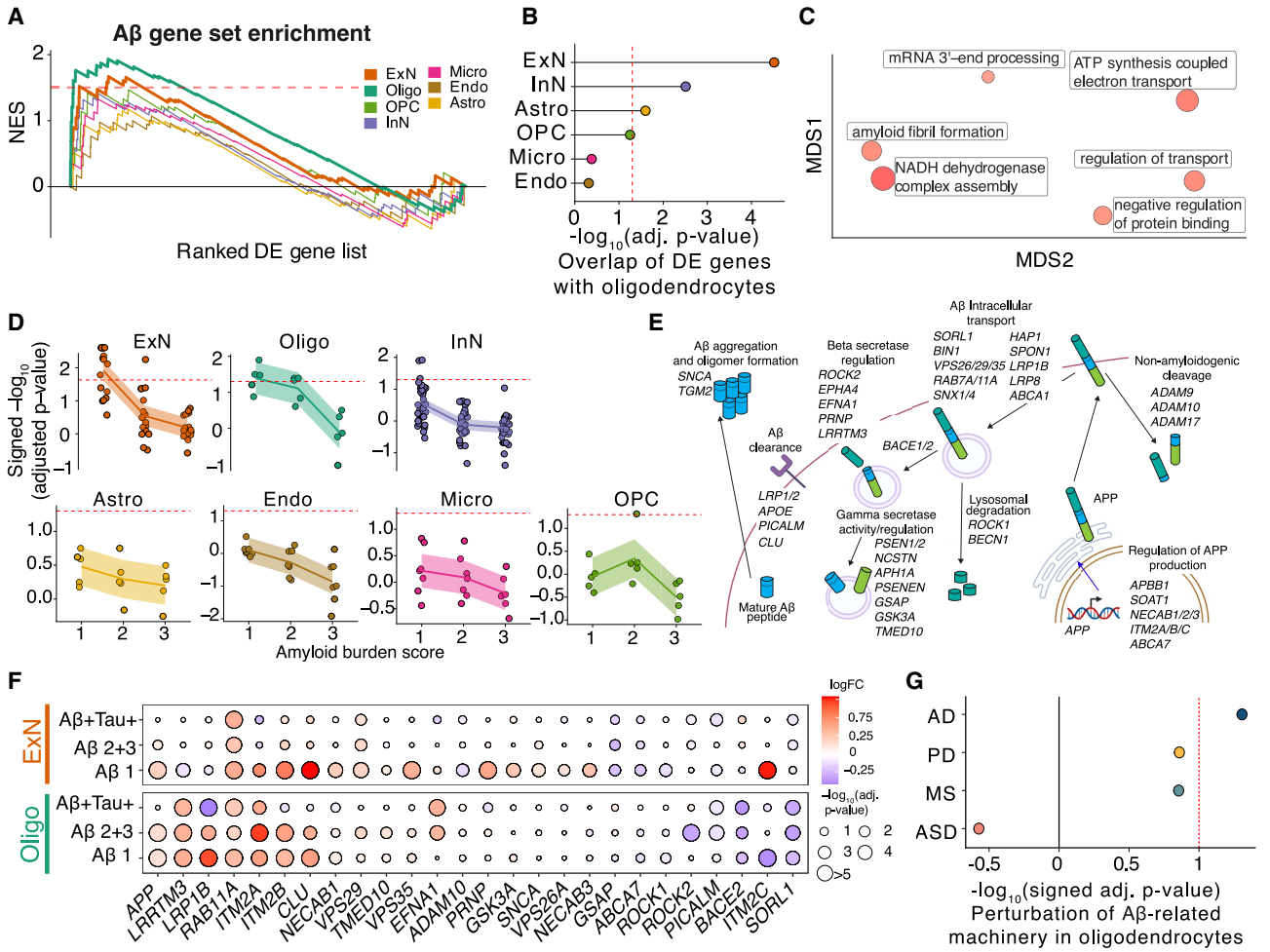

Figure 5. Cell-type-specific dysregulation of amyloid formation in the human frontal cortex

(A) GSEA trace plot of amyloid-associated gene set across the seven cell classes. The x axis shows the rank order of the DE genes (signed p value) in corresponding cell classes; the y axis is the normalized enrichment scores (NESs) from GSEA. The dashed line indicates NES score corresponding to an FDR threshold of 0.05.

(B) Dot plot of FDR-adjusted p values of GSEA results of the top 300 upregulated protein-coding genes (sorted by their jack-knifed p values) from each cell class against an ordered list of DE genes in oligodendrocytes. Dotted red line indicates the FDR threshold of 0.05.

(C) Gene ontology terms significantly enriched in intersect of DE genes between oligodendrocytes and excitatory neurons from REVIGO.[48] Size of dots denote significance. MDS, multi-dimensional scaling.

(D) GSEA results of amyloid gene set against cell-type level DE genes across increasing levels of Aβ and tau burden. Cell types are grouped based on their major cell class annotations. The dashed line represents the FDR threshold of 0.05.

(E) Schematic of the amyloid metabolism pathway. See also Table S5. Shaded bars indicate standard error.

(F) ExN and Oligo DE results across increasing levels of Aβ and tau burden for genes found by the leading-edge analysis in (A).

(G) GSEA results for the amyloid gene set on Oligo DE genes from postmortem AD, PD, MS, and ASD cohorts.

See also Figure S6.

oligodendrocyte-derived Aβ peptides could contribute to AD-related amyloidosis in similar ways to ExNs.

DISCUSSION

Therapeutic trials of AD have made increasingly clear the importance of early intervention in the disease,[2] but identifying the cellular states occurring in human tissue at early disease stages has been challenging. Here, we leveraged a unique cohort of fresh human brain biopsy tissue to identify cellular perturbations—which we collectively refer to as the ECAR—that are specifically present in tissue at the earliest stages of AD pathology. One prominent ECAR component was the identification of a hyperactive, hypermetabolic signature within ExNs, which was confirmed in an independent cohort by slice electrophysiology. It was also associated with an astrocytic upregulation of glutathione metabolism and fatty acid degradation, suggesting dysregulation of synapse homeostasis in response to aberrant neuronal activity.[34,35] Furthermore, this upper-layer hyperactivity phenotype was tightly coupled with the loss of a specific *NDNF*-expressing

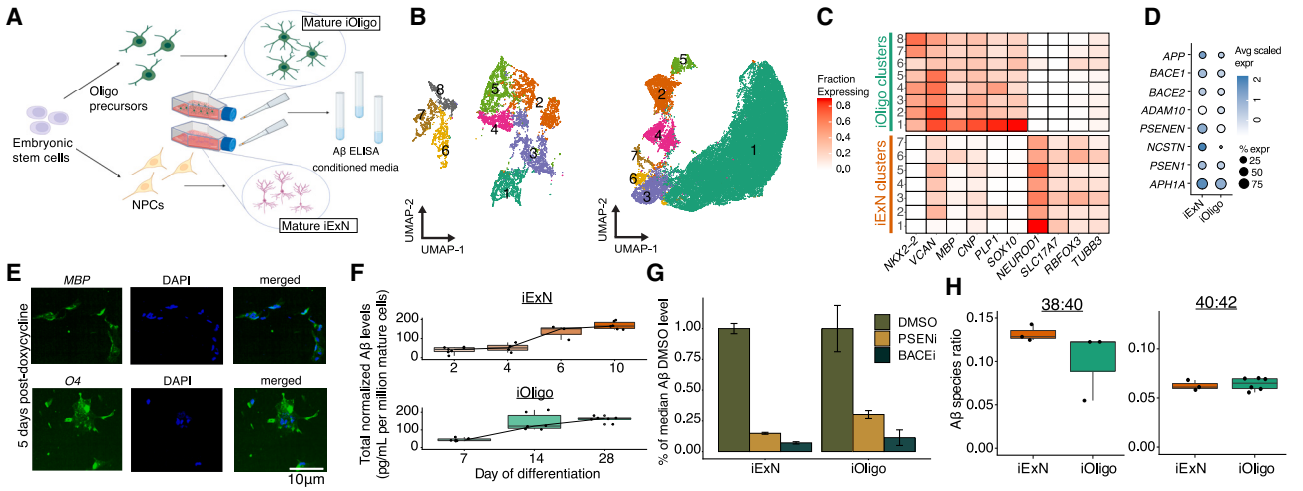

Figure 6. Quantitation of Aβ production by human mature iOligo and iExN cultures

(A) Schematic of experiments performed with iOligos and iExN cultures. NPCs, neural progenitor cells.

(B) Two-dimensional representation of single-cell expression profiles obtained from iOligo (left) and iExN (right) differentiation protocols.

(C and D) Expressions of key marker genes (C) and Aβ processing genes (D) in iOligo and iExN cultures.

(E) Immunofluorescence stains of *O4* and *MBP* in iOligo cultures 5 days after doxycycline addition.

(F) Normalized Aβ protein abundance for iExNs (top) and iOligos (bottom) across differentiation.

(G) Fractional abundance of Aβ protein levels relative to median Aβ protein levels in DMSO condition for presenillin (PSEN) inhibitor-treated and BACE inhibitor-treated conditioned media samples for iOligos and iExNs. Error bars indicate one SD above and below the mean.

(H) Ratio of Aβ-38 to Aβ-40 (left) and Aβ-40 to Aβ-42 (right) species from culture conditioned media. In all panels with boxplots, Center line, median; box limits, upper and lower quartiles; whiskers, 1.5× interquartile range; points, outliers.

See also Figure S7.

L1 interneuron population early in disease progression. *NDNF*-expressing interneurons are most active in states of arousal,[25] and their activation is positively correlated with associative learning,[53] suggesting that their loss may directly affect memory formation. In addition, a recent study of *NDNF*-expressing neurons in the hippocampus found that their potentiation led to an inhibitory shift at excitatory synapses between entorhinal cortical projections and CA1 neuronal dendrites.[54] The loss of this cell type could thus help seed foci of aberrant excitation, further aggravating the acute effects of Aβ accumulation in the tissue. Hyperactivity has been observed in animal AD models that either overexpress APP or are exposed to Aβ-containing extracts from AD patients.[32,34,55,56] In addition, measurement of synaptic markers in postmortem brains from AD-affected individuals indicates an increased excitatory-to-inhibitory ratio in temporal and parietal cortices, favoring hyperexcitability.[57,58] Our work in human tissue finds that hyperactivity is a prelude to subsequent upper layer ExN loss and postulates a mechanism—loss of a specific InN population—that could contribute to its onset.

The second ECAR component is the expansion of two activated microglial states, one of which (GPNMB-EYA2) is shared between AD and PD and the other (LPL-CD83) is expanded only in AD. One means by which microglia protect against neurodegeneration is through the autophagy-mediated clearance of Aβ[59] and α-synuclein,[60] a convergence that could explain the expansion of the GPNMB-EYA2 population—enriched for autophagy-related genes—in both AD and PD. The LPL-CD83 population—whose expansion is AD-specific—shows high expression of TGF-β signaling components, including *TGFBR1* and *SMAD3*, which both promote Aβ clearance by microglia[61] and mediate tissue repair.[62] According to our integrative analysis, neither of these cell states was expanded in the examined AD mouse models, and the states themselves showed more molecular divergence between species than other microglial states, arguing for the importance of human samples when studying these highly disease-relevant cells. Interestingly, exposure of human ESC-derived microglia to diverse brain-related challenges was recently shown to induce *in vitro* cellular states that transcriptionally resemble our *GPNMB+* states (e.g., high expression of *GLDN*, *CD83*, *PPARG*, and *MYO1E*).[63] It will be important to more deeply characterize these states genomically and to study their functional properties, such as capacity for phagocytosis, synaptic engulfment, and neuroinflammatory potential.

The last ECAR component we identified was a shared signature, in both oligodendrocytes and excitatory neurons, of differentially regulated genes associated with Aβ production. This signature peaked, especially in the earliest stages of Aβ deposition.[64] Because our signature derives from measurements made from human biopsy tissue, it provided us with a unique opportunity to uncover the molecular mechanisms underlying excess production and accumulation of Aβ in early stages of AD pathology in the human brain. Upregulated genes in this signature encoded for pro-amyloidogenic factors such as *LRRTM3*, and *RAB11A*, as well as *APP* itself, whereas *ITM2B*, *SORL1*, and *BACE2* were downregulated. The misregulation of these specific genes within human diseased tissue nominates them as especially promising targets for therapeutic intervention into early β-amyloid accumulation.

Prior work in animal cells and models has suggested that other cell types, beyond ExNs, could be sources of amyloid.[65,66] Our *in vivo* and *in vitro* analyses indicate that in humans, Aβ production is possible in both oligodendrocytes and excitatory neurons. We further utilized our human culture system to validate functionality of the β-amyloid pathway by way of chemical knockdowns of key enzymatic proteins. Neuropathological studies have postulated an inverse relationship between myelination and AD pathology,[67] prompting hypotheses that myelin breakdown may play a causal role in the disease.[68] Additionally, white matter regions are some of the first to exhibit a high burden of oligomeric Aβ.[69] These studies, coupled with our results, underscore the relevance of the interface between neuronal axons and oligodendrocytic bodies to AD pathogenesis.

Our integrative analysis illustrates that cell-type identities are more resilient to peri- and postmortem effects compared with expression patterns of individual genes and can be accurately recovered by anchoring to high-quality datasets. From this work, we conclude that single-cell brain datasets are generally of sufficient consistency and quality that it is possible to conduct cumulative, highly informative meta-analyses. Such analyses will not only ensure the consistency of biological findings across multiple cohorts but also enable comparative analyses—as we performed here—to assess the specificity of a state for a particular disease. To further facilitate this endeavor, we have established a web-based resource (available at https://braincelldata.org/resource) where individual scientists can align their own data with our integrative analysis, providing a common language for understanding cell-type-specific changes in different diseases. We expect that the continued accrual of data from more donors, regions, species, and related conditions will provide additional crucial insights into the pathogenic process of AD and other diseases of the brain.

Limitations of the study

Our study necessarily focused on cell states and cell loss associated with AD pathology in the frontal cortex, owing to the limitations of obtaining fresh biopsy tissue from other brain areas. Additional experiments—potentially leveraging cell-type-specific proteomic labeling[70,71] or laser capture microdissection—will be needed to definitively establish the contribution of specific cell types to amyloid production. Finally, neuronal transcriptional states appear to be less well preserved in postmortem tissue, and hence, more mechanistic studies of the hyperactivity state that precedes neuronal loss may particularly require the use of acute biopsy slices as well as select cellular and animal models.

STAR★METHODS

Detailed methods are provided in the online version of this paper and include the following:

- KEY RESOURCES TABLE
- RESOURCE AVAILABILITY
  - Lead contact
  - Materials availability
  - Data and code availability
- EXPERIMENTAL MODEL AND STUDY PARTICIPANT DETAILS
  - Primary biopsy cohort
  - Validation cohort
  - Cell lines
- METHOD DETAILS
  - Procurement of frontal cortex brain biopsies
  - Neuroanatomical localization of biopsy site
  - Biopsy tissue quality scoring
  - Measurement of iNPH grading scale and clinical diagnosis
  - Generation of single-nuclei suspensions from frozen brain biopsies
  - Single-nucleus and single-cell RNA-sequencing and read pre-processing
  - Initial clustering of the biopsy cohort
  - Integrative analysis of the biopsy dataset with postmortem studies
  - Cell type marker analysis
  - Differential abundance analysis
  - Differential gene expression analysis
  - Gene set enrichment analysis
  - Correlating cell-type-proportional changes to transcriptome responses across cell types
  - Heritability enrichment of differentially expressed genes with MAGMA
  - Brain slice preparation for electrophysiological experiments
  - 3D-multielectrode array electrophysiology
  - 3D-MEA data analysis
  - Histological determinations and immunohistochemistry
  - Generation of a doxycycline-inducible *SOX10* H1 stem cell line
  - Oligodendrocyte differentiation of ESCs
  - Neuronal differentiation of ESCs
  - Immunohistochemistry and imaging of ESCs
  - Generation of single-cell suspension from ESC-derived H1 iOligodendrocytes
  - Read processing and clustering of iOligodendrocyte and iExcitatory Neuron scRNA-seq experiments
  - ELISA-based amyloid beta quantification
- QUANTIFICATION AND STATISTICAL ANALYSIS

SUPPLEMENTAL INFORMATION

Supplemental information can be found online at https://doi.org/10.1016/j.cell.2023.08.005.

ACKNOWLEDGMENTS

We would like to thank Henrik Zetterberg, Nader Morshed, and Michael-John Dolan for helpful discussions. We are also grateful for the help of Marita Parviainen and Tiina Laaksonen with patient management and cognitive testing as well as Andrea Jiang with performing the β-amyloid ELISA assays. We thank Mirka Tikkanen for technical expertise for tissue immunohistochemistry. We also thank Henna Jantti for the schematic representation of brain biopsy procedure and acute slice physiology experiments. This work was supported by the Alzheimer's Association and the International Neuroimmune Consortium (to B.S. and E.Z.M.), the Pew Biomedical Scholars Program (to E.Z.M.), NIH NIGMS grants T32GM007753/T32GM144273 (to T.K.), NIH NIA grant

F30AG069446 (to T.K.), and the Kuopio University Hospital VTR fund (grant 5252614 to V.L.), Academy of Finland (grants 339763 and 334801 to T.M. and 338182 and 328287 to M.H.), the Sigrid Juselius Foundation, the Strategic Neuroscience Funding of the University of Eastern Finland, the Finnish Cultural Foundation, and the North Savo Regional Fund and by the European Union (ERC, HUMANE, and 101043584 to T.M.). Views and opinions expressed are those of the author(s) only and do not necessarily reflect those of the European Union or the European Research Council Executive Agency. Neither the European Union nor the granting authority can be held responsible for them.

AUTHOR CONTRIBUTIONS

V.G. and T.K. performed all analyses with help from A.J. and S.E.M. N.M.N. generated the snRNA-seq data with help from T.K., C.V., and A.A. V.L. conceived, designed, and oversaw the construction of the biopsy cohort with help from M.H. and T.M. A.M.K. conducted the longitudinal assessment of clinical records with help from A.J. A.D., A.P., M.G.-B., and N.-N.V. conducted the electrophysiological experiments. A.D. analyzed electrophysiological data with help from V.G. T.K., B.R., M. Therrien, M. Tegtmeyer, and R.N. performed the differentiated stem cell experiments. T.R. pathologically staged the biopsies, and S.-K.H. collected the CSF from patients. T.M. oversaw the electrophysiological experiments. B.S., V.L., and E.Z.M. conceived of the study. V.G., T.K., and E.Z.M. wrote the paper with contributions from all authors.

DECLARATION OF INTERESTS

The authors declare no competing interests.

Received: January 11, 2023
Revised: May 31, 2023
Accepted: August 3, 2023
Published: September 28, 2023

REFERENCES

1. De Strooper, B., and Karran, E. (2016). The cellular phase of Alzheimer's disease. Cell *164*, 603–615.
2. Long, J.M., and Holtzman, D.M. (2019). Alzheimer disease: an update on pathobiology and treatment strategies. Cell *179*, 312–339.
3. Mathys, H., Davila-Velderrain, J., Peng, Z., Gao, F., Mohammadi, S., Young, J.Z., Menon, M., He, L., Abdurrob, F., Jiang, X., et al. (2019). Single-cell transcriptomic analysis of Alzheimer's disease. Nature *570*, 332–337.
4. Leng, K., Li, E., Eser, R., Piergies, A., Sit, R., Tan, M., Neff, N., Li, S.H., Rodriguez, R.D., Suemoto, C.K., et al. (2021). Molecular characterization of selectively vulnerable neurons in Alzheimer's disease. Nat. Neurosci. *24*, 276–287.
5. Lau, S.F., Cao, H., Fu, A.K.Y., and Ip, N.Y. (2020). Single-nucleus transcriptome analysis reveals dysregulation of angiogenic endothelial cells and neuroprotective glia in Alzheimer's disease. Proc. Natl. Acad. Sci. USA *117*, 25800–25809.
6. Gerrits, E., Brouwer, N., Kooistra, S.M., Woodbury, M.E., Vermeiren, Y., Lambourne, M., Mulder, J., Kummer, M., Möller, T., Biber, K., et al. (2021). Distinct amyloid-β and tau-associated microglia profiles in Alzheimer's disease. Acta Neuropathol. *141*, 681–696.
7. Otero-Garcia, M., Mahajani, S.U., Wakhloo, D., Tang, W., Xue, Y.Q., Morabito, S., Pan, J., Oberhauser, J., Madira, A.E., Shakouri, T., et al. (2022). Molecular signatures underlying neurofibrillary tangle susceptibility in Alzheimer's disease. Neuron *110*, 2929–2948.e8.
8. Marinaro, F., Haneklaus, M., Zhang, Z., Strano, A., Evans, L., Handfield, L.-F., Ryan, N.S., Fox, N.C., Hemberg, M., Ramanathan, S., et al. (2020). Molecular and cellular pathology of monogenic Alzheimer's disease at single cell resolution. Preprint at bioRxiv. https://doi.org/10.1101/2020.07.14.202317.
9. Kramvis, I., Mansvelder, H.D., and Meredith, R.M. (2018). Neuronal life after death: electrophysiologic recordings from neurons in adult human brain tissue obtained through surgical resection or postmortem. Handb. Clin. Neurol. *150*, 319–333.
10. Guo, L., Rezvanian, A., Kukreja, L., Hoveydai, R., Bigio, E.H., Mesulam, M.M., El Khoury, J., and Geula, C. (2016). Postmortem adult human microglia proliferate in culture to high passage and maintain their response to amyloid-β. J. Alzheimers Dis. *54*, 1157–1167.
11. De Groot, C.J., Montagne, L., Janssen, I., Ravid, R., Van Der Valk, P., and Veerhuis, R. (2000). Isolation and characterization of adult microglial cells and oligodendrocytes derived from postmortem human brain tissue. Brain Res. Brain Res. Protoc. *5*, 85–94.
12. Dachet, F., Brown, J.B., Valyi-Nagy, T., Narayan, K.D., Serafini, A., Boley, N., Gingeras, T.R., Celniker, S.E., Mohapatra, G., and Loeb, J.A. (2021). Selective time-dependent changes in activity and cell-specific gene expression in human postmortem brain. Sci. Rep. *11*, 6078.
13. Luikku, A.J., Hall, A., Nerg, O., Koivisto, A.M., Hiltunen, M., Helisalmi, S., Herukka, S.K., Junkkari, A., Sutela, A., Kojoukhova, M., et al. (2019). Predicting development of Alzheimer's disease in patients with shunted idiopathic normal pressure hydrocephalus. J. Alzheimers Dis. *71*, 1233–1243.
14. Leinonen, V., Koivisto, A.M., Alafuzoff, I., Pyykkö, O.T., Rummukainen, J., von Und Zu Fraunberg, M., Jääskeläinen, J.E., Soininen, H., Rinne, J., and Savolainen, S. (2012). Cortical brain biopsy in long-term prognostication of 468 patients with possible normal pressure hydrocephalus. Neurodegener. Dis. *10*, 166–169.
15. Hamilton, R., Patel, S., Lee, E.B., Jackson, E.M., Lopinto, J., Arnold, S.E., Clark, C.M., Basil, A., Shaw, L.M., Xie, S.X., et al. (2010). Lack of shunt response in suspected idiopathic normal pressure hydrocephalus with Alzheimer disease pathology. Ann. Neurol. *68*, 535–540.
16. Seeburger, J.L., Holder, D.J., Combrinck, M., Joachim, C., Laterza, O., Tanen, M., Dallob, A., Chappell, D., Snyder, K., Flynn, M., et al. (2015). Cerebrospinal fluid biomarkers distinguish postmortem-confirmed Alzheimer's disease from other dementias and healthy controls in the OPTIMA cohort. J. Alzheimers Dis. *44*, 525–539.
17. Strozyk, D., Blennow, K., White, L.R., and Launer, L.J. (2003). CSF Abeta 42 levels correlate with amyloid-neuropathology in a population-based autopsy study. Neurology *60*, 652–656.
18. Welch, J.D., Kozareva, V., Ferreira, A., Vanderburg, C., Martin, C., and Macosko, E.Z. (2019). Single-cell multi-omic integration compares and contrasts features of brain cell identity. Cell *177*, 1873–1887.e17.
19. Marsh, S.E., Walker, A.J., Kamath, T., Dissing-Olesen, L., Hammond, T.R., de Soysa, T.Y., Young, A.M.H., Murphy, S., Abdulraouf, A., Nadaf, N., et al. (2022). Dissection of artifactual and confounding glial signatures by single-cell sequencing of mouse and human brain. Nat. Neurosci. *25*, 306–316.
20. Wu, Y.E., Pan, L., Zuo, Y., Li, X., and Hong, W. (2017). Detecting activated cell populations using single-cell RNA-seq. Neuron *96*, 313–329.e6.
21. Bakken, T.E., Jorstad, N.L., Hu, Q., Lake, B.B., Tian, W., Kalmbach, B.E., Crow, M., Hodge, R.D., Krienen, F.M., Sorensen, S.A., et al. (2021). Comparative cellular analysis of motor cortex in human, marmoset and mouse. Nature *598*, 111–119.
22. Habib, N., McCabe, C., Medina, S., Varshavsky, M., Kitsberg, D., Dvir-Szternfeld, R., Green, G., Dionne, D., Nguyen, L., Marshall, J.L., et al. (2020). Disease-associated astrocytes in Alzheimer's disease and aging. Nat. Neurosci. *23*, 701–706.
23. Tyssowski, K.M., DeStefino, N.R., Cho, J.H., Dunn, C.J., Poston, R.G., Carty, C.E., Jones, R.D., Chang, S.M., Romeo, P., Wurzelmann, M.K., et al. (2018). Different neuronal activity patterns induce different gene expression programs. Neuron *98*, 530–546.e11.
24. Ibrahim, L.A., Huang, S., Fernandez-Otero, M., Sherer, M., Qiu, Y., Vemuri, S., Xu, Q., Machold, R., Pouchelon, G., Rudy, B., et al. (2021).

Bottom-up inputs are required for establishment of top-down connectivity onto cortical layer 1 neurogliaform cells. Neuron *109*, 3473–3485.e5.

25. Cohen-Kashi Malina, K.C.-K., Tsivourakis, E., Kushinsky, D., Apelblat, D., Shtiglitz, S., Zohar, E., Sokoletsky, M., Tasaka, G.I., Mizrahi, A., Lampl, I., et al. (2021). NDNF interneurons in layer 1 gain-modulate whole cortical columns according to an animal's behavioral state. Neuron *109*, 2150–2164.e5. https://doi.org/10.1016/j.neuron.2021.05.001.
26. West, A.E., and Greenberg, M.E. (2011). Neuronal activity-regulated gene transcription in synapse development and cognitive function. Cold Spring Harb. Perspect. Biol. *3*. https://doi.org/10.1101/cshperspect.a005744.
27. Turrigiano, G.G. (2008). The self-tuning neuron: synaptic scaling of excitatory synapses. Cell *135*, 422–435.
28. Verderio, C., Pozzi, D., Pravettoni, E., Inverardi, F., Schenk, U., Coco, S., Proux-Gillardeaux, V., Galli, T., Rossetto, O., Frassoni, C., et al. (2004). SNAP-25 modulation of calcium dynamics underlies differences in GABAergic and glutamatergic responsiveness to depolarization. Neuron *41*, 599–610.
29. Pozzi, D., Condliffe, S., Bozzi, Y., Chikhladze, M., Grumelli, C., Proux-Gillardeaux, V., Takahashi, M., Franceschetti, S., Verderio, C., and Matteoli, M. (2008). Activity-dependent phosphorylation of Ser187 is required for SNAP-25-negative modulation of neuronal voltage-gated calcium channels. Proc. Natl. Acad. Sci. USA *105*, 323–328.
30. Kim, S.H., and Ryan, T.A. (2010). CDK5 serves as a major control point in neurotransmitter release. Neuron *67*, 797–809.
31. Cirrito, J.R., Yamada, K.A., Finn, M.B., Sloviter, R.S., Bales, K.R., May, P.C., Schoepp, D.D., Paul, S.M., Mennerick, S., and Holtzman, D.M. (2005). Synaptic activity regulates interstitial fluid amyloid-beta levels in vivo. Neuron *48*, 913–922.
32. Li, S., and Selkoe, D.J. (2020). A mechanistic hypothesis for the impairment of synaptic plasticity by soluble Aβ oligomers from Alzheimer's brain. J. Neurochem. *154*, 583–597.
33. Ohnishi, T., Yanazawa, M., Sasahara, T., Kitamura, Y., Hiroaki, H., Fukazawa, Y., Kii, I., Nishiyama, T., Kakita, A., Takeda, H., et al. (2015). Na, K-ATPase α3 is a death target of Alzheimer patient amyloid-β assembly. Proc. Natl. Acad. Sci. USA *112*, E4465–E4474.
34. Zott, B., Simon, M.M., Hong, W., Unger, F., Chen-Engerer, H.J., Frosch, M.P., Sakmann, B., Walsh, D.M., and Konnerth, A. (2019). A vicious cycle of β amyloid-dependent neuronal hyperactivation. Science *365*, 559–565.
35. Ioannou, M.S., Jackson, J., Sheu, S.H., Chang, C.L., Weigel, A.V., Liu, H., Pasolli, H.A., Xu, C.S., Pang, S., Matthies, D., et al. (2019). Neuron-astrocyte metabolic coupling protects against activity-induced fatty acid toxicity. Cell *177*, 1522–1535.e14.
36. Wightman, D.P., Jansen, I.E., Savage, J.E., Shadrin, A.A., Bahrami, S., Holland, D., Rongve, A., Børte, S., Winsvold, B.S., Drange, O.K., et al. (2021). A genome-wide association study with 1,126,563 individuals identifies new risk loci for Alzheimer's disease. Nat. Genet. *53*, 1276–1282.
37. Bellenguez, C., Küçükali, F., Jansen, I.E., Kleineidam, L., Moreno-Grau, S., Amin, N., Naj, A.C., Campos-Martin, R., Grenier-Boley, B., Andrade, V., et al. (2022). New insights into the genetic etiology of Alzheimer's disease and related dementias. Nat. Genet. *54*, 412–436.
38. Jansen, I.E., Savage, J.E., Watanabe, K., Bryois, J., Williams, D.M., Steinberg, S., Sealock, J., Karlsson, I.K., Hägg, S., Athanasiu, L., et al. (2019). Genome-wide meta-analysis identifies new loci and functional pathways influencing Alzheimer's disease risk. Nat. Genet. *51*, 404–413.
39. Mich, J.K., Graybuck, L.T., Hess, E.E., Mahoney, J.T., Kojima, Y., Ding, Y., Somasundaram, S., Miller, J.A., Kalmbach, B.E., Radaelli, C., et al. (2021). Functional enhancer elements drive subclass-selective expression from mouse to primate neocortex. Cell Rep. *34*, 108754.
40. Keren-Shaul, H., Spinrad, A., Weiner, A., Matcovitch-Natan, O., Dvir-Szternfeld, R., Ulland, T.K., David, E., Baruch, K., Lara-Astaiso, D., Toth, B., et al. (2017). A unique microglia type associated with restricting development of Alzheimer's disease. Cell *169*, 1276–1290.e17.
41. Li, Q., Cheng, Z., Zhou, L., Darmanis, S., Neff, N.F., Okamoto, J., Gulati, G., Bennett, M.L., Sun, L.O., Clarke, L.E., et al. (2019). Developmental heterogeneity of microglia and brain myeloid cells revealed by deep single-cell RNA sequencing. Neuron *101*, 207–223.e10.
42. Lopes, K.P., Snijders, G.J.L., Humphrey, J., Allan, A., Sneeboer, M.A.M., Navarro, E., Schilder, B.M., Vialle, R.A., Parks, M., Missall, R., et al. (2022). Genetic analysis of the human microglial transcriptome across brain regions, aging and disease pathologies. Nat. Genet. *54*, 4–17.
43. de Leeuw, C.A., Mooij, J.M., Heskes, T., and Posthuma, D. (2015). MAGMA: generalized gene-set analysis of GWAS data. PLOS Comput. Biol. *11*, e1004219.
44. Gomez-Nicola, D., Valle-Argos, B., and Nieto-Sampedro, M. (2010). Blockade of IL-15 activity inhibits microglial activation through the NFkappaB, p38, and ERK1/2 pathways, reducing cytokine and chemokine release. Glia *58*, 264–276.
45. Matejuk, A., and Ransohoff, R.M. (2020). Crosstalk between astrocytes and microglia: an overview. Front. Immunol. *11*, 1416. https://doi.org/10.3389/fimmu.2020.01416.
46. Shi, S.X., Li, Y.J., Shi, K., Wood, K., Ducruet, A.F., and Liu, Q. (2020). IL (interleukin)-15 bridges astrocyte-microglia crosstalk and exacerbates brain injury following intracerebral hemorrhage. Stroke *51*, 967–974.
47. Girskis, K.M., Stergachis, A.B., DeGennaro, E.M., Doan, R.N., Qian, X., Johnson, M.B., Wang, P.P., Sejourne, G.M., Nagy, M.A., Pollina, E.A., et al. (2021). Rewiring of human neurodevelopmental gene regulatory programs by human accelerated regions. Neuron *109*, 3239–3251.e7.
48. Supek, F., Bošnjak, M., Škunca, N., and Šmuc, T. (2011). REVIGO summarizes and visualizes long lists of gene ontology terms. PLoS One *6*, e21800.
49. Kamath, T., Abdulraouf, A., Burris, S.J., Langlieb, J., Gazestani, V., Nadaf, N.M., Balderrama, K., Vanderburg, C., and Macosko, E.Z. (2022). Single-cell genomic profiling of human dopamine neurons identifies a population that selectively degenerates in Parkinson's disease. Nat. Neurosci. *25*, 588–595.
50. Smajić, S., Prada-Medina, C.A., Landoulsi, Z., Ghelfi, J., Delcambre, S., Dietrich, C., Jarazo, J., Henck, J., Balachandran, S., Pachchek, S., et al. (2022). Single-cell sequencing of human midbrain reveals glial activation and a Parkinson-specific neuronal state. Brain *145*, 964–978.
51. Velmeshev, D., Schirmer, L., Jung, D., Haeussler, M., Perez, Y., Mayer, S., Bhaduri, A., Goyal, N., Rowitch, D.H., and Kriegstein, A.R. (2019). Single-cell genomics identifies cell type-specific molecular changes in autism. Science *364*, 685–689.
52. Jäkel, S., Agirre, E., Mendanha Falcão, A., van Bruggen, D., Lee, K.W., Knuesel, I., Malhotra, D., Ffrench-Constant, C., Williams, A., and Castelo-Branco, G. (2019). Altered human oligodendrocyte heterogeneity in multiple sclerosis. Nature *566*, 543–547.
53. Abs, E., Poorthuis, R.B., Apelblat, D., Muhammad, K., Pardi, M.B., Enke, L., Kushinsky, D., Pu, D.L., Eizinger, M.F., Conzelmann, K.K., et al. (2018). Learning-related plasticity in dendrite-targeting Layer 1 interneurons. Neuron *100*, 684–699.e6.
54. Mercier, M.S., Magloire, V., Cornford, J.H., and Kullmann, D.M. (2022). Long-term potentiation in neurogliaform interneurons modulates excitation-inhibition balance in the temporoammonic pathway. J. Physiol. *600*, 4001–4017.
55. Shah, D., Gsell, W., Wahis, J., Luckett, E.S., Jamoulle, T., Vermaercke, B., Preman, P., Moechars, D., Hendrickx, V., Jaspers, T., et al. (2022). Astrocyte calcium dysfunction causes early network hyperactivity in Alzheimer's disease. Cell Rep. *40*, 111280.
56. Busche, M.A., Eichhoff, G., Adelsberger, H., Abramowski, D., Wiederhold, K.H., Haass, C., Staufenbiel, M., Konnerth, A., and Garaschuk, O. (2008). Clusters of hyperactive neurons near amyloid plaques in a mouse model of Alzheimer's disease. Science *321*, 1686–1689.

57. Lauterborn, J.C., Scaduto, P., Cox, C.D., Schulmann, A., Lynch, G., Gall, C.M., Keene, C.D., and Limon, A. (2021). Increased excitatory to inhibitory synaptic ratio in parietal cortex samples from individuals with Alzheimer's disease. Nat. Commun. *12*, 2603.

58. Scaduto, P., Lauterborn, J.C., Cox, C.D., Fracassi, A., Zeppillo, T., Gutierrez, B.A., Keene, C.D., Crane, P.K., Mukherjee, S., Russell, W.K., et al. (2023). Functional excitatory to inhibitory synaptic imbalance and loss of cognitive performance in people with Alzheimer's disease neuropathologic change. Acta Neuropathol. *145*, 303–324.

59. Tarasoff-Conway, J.M., Carare, R.O., Osorio, R.S., Glodzik, L., Butler, T., Fieremans, E., Axel, L., Rusinek, H., Nicholson, C., Zlokovic, B.V., et al. (2015). Clearance systems in the brain-implications for Alzheimer disease. Nat. Rev. Neurol. *11*, 457–470. https://doi.org/10.1038/nrneurol.2015.119.

60. Choi, I., Zhang, Y., Seegobin, S.P., Pruvost, M., Wang, Q., Purtell, K., Zhang, B., and Yue, Z. (2020). Microglia clear neuron-released α-synuclein via selective autophagy and prevent neurodegeneration. Nat. Commun. *11*, 1386.

61. Wyss-Coray, T., Lin, C., Yan, F., Yu, G.Q., Rohde, M., McConlogue, L., Masliah, E., and Mucke, L. (2001). TGF-beta1 promotes microglial amyloid-beta clearance and reduces plaque burden in transgenic mice. Nat. Med. *7*, 612–618.

62. Brionne, T.C., Tesseur, I., Masliah, E., and Wyss-Coray, T. (2003). Loss of TGF-beta 1 leads to increased neuronal cell death and microgliosis in mouse brain. Neuron *40*, 1133–1145.

63. Dolan, M.-J., Therrien, M., Jereb, S., Kamath, T., Atkeson, T., Marsh, S.E., Goeva, A., Lojek, N.M., Murphy, S., White, C.M., et al. (2022). A resource for generating and manipulating human microglial states in vitro. Preprint at bioRxiv. https://doi.org/10.1101/2022.05.02.490100.

64. Bateman, R.J., Xiong, C., Benzinger, T.L.S., Fagan, A.M., Goate, A., Fox, N.C., Marcus, D.S., Cairns, N.J., Xie, X., Blazey, T.M., et al. (2012). Clinical and biomarker changes in dominantly inherited Alzheimer's disease. N. Engl. J. Med. *367*, 795–804.

65. Veeraraghavalu, K., Zhang, C., Zhang, X., Tanzi, R.E., and Sisodia, S.S. (2014). Age-dependent, non-cell-autonomous deposition of amyloid from synthesis of β-amyloid by cells other than excitatory neurons. J. Neurosci. *34*, 3668–3673.

66. Skaper, S.D., Evans, N.A., Evans, N.A., Rosin, C., Facci, L., and Richardson, J.C. (2009). Oligodendrocytes are a novel source of amyloid peptide generation. Neurochem. Res. *34*, 2243–2250.

67. Braak, H., and Braak, E. (1996). Development of Alzheimer-related neurofibrillary changes in the neocortex inversely recapitulates cortical myelogenesis. Acta Neuropathol. *92*, 197–201.

68. Bartzokis, G., Lu, P.H., and Mintz, J. (2007). Human brain myelination and amyloid beta deposition in Alzheimer's disease. Alzheimers Dement. *3*, 122–125.

69. Collins-Praino, L.E., Francis, Y.I., Griffith, E.Y., Wiegman, A.F., Urbach, J., Lawton, A., Honig, L.S., Cortes, E., Vonsattel, J.P.G., Canoll, P.D., et al. (2014). Soluble amyloid beta levels are elevated in the white matter of Alzheimer's patients, independent of cortical plaque severity. Acta Neuropathol. Commun. *2*, 83.

70. Yang, A.C., du Bois, H., Olsson, N., Gate, D., Lehallier, B., Berdnik, D., Brewer, K.D., Bertozzi, C.R., Elias, J.E., and Wyss-Coray, T. (2018). Multiple click-selective tRNA synthetases expand mammalian cell-specific proteomics. J. Am. Chem. Soc. *140*, 7046–7051.

71. Alvarez-Castelao, B., Schanzenbächer, C.T., Langer, J.D., and Schuman, E.M. (2019). Cell-type-specific metabolic labeling, detection and identification of nascent proteomes in vivo. Nat. Protoc. *14*, 556–575.

72. Zhou, Y., Song, W.M., Andhey, P.S., Swain, A., Levy, T., Miller, K.R., Poliani, P.L., Cominelli, M., Grover, S., Gilfillan, S., et al. (2020). Human and mouse single-nucleus transcriptomics reveal TREM2-dependent and TREM2-independent cellular responses in Alzheimer's disease. Nat. Med. *26*, 131–142.

73. Grubman, A., Chew, G., Ouyang, J.F., Sun, G., Choo, X.Y., McLean, C., Simmons, R.K., Buckberry, S., Vargas-Landin, D.B., Poppe, D., et al. (2019). A single-cell atlas of entorhinal cortex from individuals with Alzheimer's disease reveals cell-type-specific gene expression regulation. Nat. Neurosci. *22*, 2087–2097.

74. Li, M., Santpere, G., Imamura Kawasawa, Y., Evgrafov, O.V., Gulden, F.O., Pochareddy, S., Sunkin, S.M., Li, Z., Shin, Y., Zhu, Y., et al. (2018). Integrative functional genomic analysis of human brain development and neuropsychiatric risks. Science *362*. https://doi.org/10.1126/science.aat7615.

75. Lake, B.B., Chen, S., Sos, B.C., Fan, J., Kaeser, G.E., Yung, Y.C., Duong, T.E., Gao, D., Chun, J., Kharchenko, P.V., et al. (2018). Integrative single-cell analysis of transcriptional and epigenetic states in the human adult brain. Nat. Biotechnol. *36*, 70–80.

76. Habib, N., Avraham-Davidi, I., Basu, A., Burks, T., Shekhar, K., Hofree, M., Choudhury, S.R., Aguet, F., Gelfand, E., Ardlie, K., et al. (2017). Massively parallel single-nucleus RNA-seq with DroNc-seq. Nat. Methods *14*, 955–958.

77. Hodge, R.D., Bakken, T.E., Miller, J.A., Smith, K.A., Barkan, E.R., Graybuck, L.T., Close, J.L., Long, B., Johansen, N., Penn, O., et al. (2019). Conserved cell types with divergent features in human versus mouse cortex. Nature *573*, 61–68.

78. Yao, Z., Liu, H., Xie, F., Fischer, S., Adkins, R.S., Aldridge, A.I., Ament, S.A., Bartlett, A., Behrens, M.M., Van den Berge, K., et al. (2021). A transcriptomic and epigenomic cell atlas of the mouse primary motor cortex. Nature *598*, 103–110.

79. Bhattacherjee, A., Djekidel, M.N., Chen, R., Chen, W., Tuesta, L.M., and Zhang, Y. (2019). Cell type-specific transcriptional programs in mouse prefrontal cortex during adolescence and addiction. Nat. Commun. *10*, 4169.

80. Hammond, T.R., Dufort, C., Dissing-Olesen, L., Giera, S., Young, A., Wysoker, A., Walker, A.J., Gergits, F., Segel, M., Nemesh, J., et al. (2019). Single-cell RNA sequencing of microglia throughout the mouse lifespan and in the injured brain reveals complex cell-state changes. Immunity *50*, 253–271.e6.

81. Sierksma, A., Lu, A., Mancuso, R., Fattorelli, N., Thrupp, N., Salta, E., Zoco, J., Blum, D., Buée, L., De Strooper, B., et al. (2020). Novel Alzheimer risk genes determine the microglia response to amyloid-β but not to TAU pathology. EMBO Mol. Med. *12*, e10606.

82. Sala Frigerio, C., Wolfs, L., Fattorelli, N., Thrupp, N., Voytyuk, I., Schmidt, I., Mancuso, R., Chen, W.T., Woodbury, M.E., Srivastava, G., et al. (2019). The major risk factors for Alzheimer's disease: age, sex, and genes modulate the microglia response to Aβ plaques. Cell Rep. *27*, 1293–1306.e6.

83. Dulken, B.W., Buckley, M.T., Navarro Negredo, P., Saligrama, N., Cayrol, R., Leeman, D.S., George, B.M., Boutet, S.C., Hebestreit, K., Pluvinage, J.V., et al. (2019). Single-cell analysis reveals T cell infiltration in old neurogenic niches. Nature *571*, 205–210.

84. Masuda, T., Sankowski, R., Staszewski, O., Böttcher, C., Amann, L., Sagar, S., Scheiwe, C., Nessler, S., Kunz, P., van Loo, G., et al. (2019). Spatial and temporal heterogeneity of mouse and human microglia at single-cell resolution. Nature *566*, 388–392.

85. Zywitza, V., Misios, A., Bunatyan, L., Willnow, T.E., and Rajewsky, N. (2018). Single-cell transcriptomics characterizes cell types in the subventricular zone and uncovers molecular defects impairing adult neurogenesis. Cell Rep. *25*, 2457–2469.e8.

86. Chen, R., Wu, X., Jiang, L., and Zhang, Y. (2017). Single-cell RNA-seq reveals hypothalamic cell diversity. Cell Rep. *18*, 3227–3241.

87. Watanabe, K., Taskesen, E., van Bochoven, A., and Posthuma, D. (2017). Functional mapping and annotation of genetic associations with FUMA. Nat. Commun. *8*, 1826.

88. Macosko, E.Z., Basu, A., Satija, R., Nemesh, J., Shekhar, K., Goldman, M., Tirosh, I., Bialas, A.R., Kamitaki, N., Martersteck, E.M., et al. (2015).

Highly parallel genome-wide expression profiling of individual cells using nanoliter droplets. Cell *161*, 1202–1214.

89. Stirling, D.R., Swain-Bowden, M.J., Lucas, A.M., Carpenter, A.E., Cimini, B.A., and Goodman, A. (2021). CellProfiler 4: improvements in speed, utility and usability. BMC Bioinformatics *22*, 433.
90. Junkkari, A., Luikku, A.J., Danner, N., Jyrkkänen, H.K., Rauramaa, T., Korhonen, V.E., Koivisto, A.M., Nerg, O., Kojoukhova, M., Huttunen, T.J., et al. (2019). The Kuopio idiopathic normal pressure hydrocephalus protocol: initial outcome of 175 patients. Fluids Barriers CNS *16*, 21.
91. Seppälä, T.T., Nerg, O., Koivisto, A.M., Rummukainen, J., Puli, L., Zetterberg, H., Pyykkö, O.T., Helisalmi, S., Alafuzoff, I., Hiltunen, M., et al. (2012). CSF biomarkers for Alzheimer disease correlate with cortical brain biopsy findings. Neurology *78*, 1568–1575.
92. Leinonen, V., Koivisto, A.M., Savolainen, S., Rummukainen, J., Sutela, A., Vanninen, R., Jääskeläinen, J.E., Soininen, H., and Alafuzoff, I. (2012). Post-mortem findings in 10 patients with presumed normal-pressure hydrocephalus and review of the literature. Neuropathol. Appl. Neurobiol. *38*, 72–86.
93. Evans, A.C., Janke, A.L., Collins, D.L., and Baillet, S. (2012). Brain templates and atlases. Neuroimage *62*, 911–922.
94. Eickhoff, S.B., Stephan, K.E., Mohlberg, H., Grefkes, C., Fink, G.R., Amunts, K., and Zilles, K. (2005). A new SPM toolbox for combining probabilistic cytoarchitectonic maps and functional imaging data. Neuroimage *25*, 1325–1335.
95. Amunts, K., Mohlberg, H., Bludau, S., and Zilles, K. (2020). Julich-Brain: a 3D probabilistic atlas of the human brain's cytoarchitecture. Science *369*, 988–992. https://doi.org/10.1126/science.abb4588.
96. Kubo, Y., Kazui, H., Yoshida, T., Kito, Y., Kimura, N., Tokunaga, H., Ogino, A., Miyake, H., Ishikawa, M., and Takeda, M. (2008). Validation of grading scale for evaluating symptoms of idiopathic normal-pressure hydrocephalus. Dement. Geriatr. Cogn. Disord. *25*, 37–45.
97. Fleming, S.J., Chaffin, M.D., Arduini, A., Akkad, A.-D., Banks, E., Marioni, J.C., Philippakis, A.A., Ellinor, P.T., and Babadi, M. (2019). Unsupervised removal of systematic background noise from droplet-based single-cell experiments using CellBender. Nat. Methods. https://doi.org/10.1038/s41592-023-01943-7.
98. Blake, J.A., Baldarelli, R., Kadin, J.A., Richardson, J.E., Smith, C.L., and Bult, C.J.; Mouse Genome Database Group (2021). Mouse Genome Database (MGD): Knowledgebase for mouse-human comparative biology. Nucleic Acids Res. *49*, D981–D987.
99. Stuart, T., Butler, A., Hoffman, P., Hafemeister, C., Papalexi, E., Mauck, W.M., 3rd, Hao, Y., Stoeckius, M., Smibert, P., and Satija, R. (2019). Comprehensive integration of single-cell data. Cell *177*, 1888–1902.e21.
100. Korsunsky, I., Millard, N., Fan, J., Slowikowski, K., Zhang, F., Wei, K., Baglaenko, Y., Brenner, M., Loh, P.R., and Raychaudhuri, S. (2019). Fast, sensitive and accurate integration of single-cell data with Harmony. Nature *16*, 1289–1296.
101. van Dijk, D., Sharma, R., Nainys, J., Yim, K., Kathail, P., Carr, A.J., Burdziak, C., Moon, K.R., Chaffer, C.L., Pattabiraman, D., et al. (2018). Recovering gene interactions from single-cell data using data diffusion. Cell *174*, 716–729.e27.
102. Fonseka, C.Y., Rao, D.A., Teslovich, N.C., Korsunsky, I., Hannes, S.K., Slowikowski, K., Gurish, M.F., Donlin, L.T., Lederer, J.A., Weinblatt, M.E., et al. (2018). Mixed-effects association of single cells identifies an expanded effector CD4+ T cell subset in rheumatoid arthritis. Sci. Transl. Med. *10*. https://doi.org/10.1126/scitranslmed.aaq0305.
103. Zimmerman, K.D., Espeland, M.A., and Langefeld, C.D. (2021). A practical solution to pseudoreplication bias in single-cell studies. Nat. Commun. *12*, 738.
104. Law, C.W., Chen, Y., Shi, W., and Smyth, G.K. (2014). voom: precision weights unlock linear model analysis tools for RNA-seq read counts. Genome Biol. *15*, R29.
105. Chen, E.Y., Tan, C.M., Kou, Y., Duan, Q., Wang, Z., Meirelles, G.V., Clark, N.R., and Ma'ayan, A. (2013). Enrichr: interactive and collaborative HTML5 gene list enrichment analysis tool. BMC Bioinformatics *14*, 128.
106. Korotkevich, G., Sukhov, V., Budin, N., Shpak, B., Artyomov, M.N., and Sergushichev, A. (2021). Fast gene set enrichment analysis. Preprint at bioRxiv. https://doi.org/10.1101/060012.
107. Ding, J., Adiconis, X., Simmons, S.K., Kowalczyk, M.S., Hession, C.C., Marjanovic, N.D., Hughes, T.K., Wadsworth, M.H., Burks, T., Nguyen, L.T., et al. (2020). Systematic comparison of single-cell and single-nucleus RNA-sequencing methods. Nat. Biotechnol. *38*, 737–746.
108. Langfelder, P., and Horvath, S. (2008). WGCNA: an R package for weighted correlation network analysis. BMC Bioinformatics *9*, 559.
109. Nalls, M.A., Blauwendraat, C., Vallerga, C.L., Heilbron, K., Bandres-Ciga, S., Chang, D., Tan, M., Kia, D.A., Noyce, A.J., Xue, A., et al. (2019). Identification of novel risk loci, causal insights, and heritable risk for Parkinson's disease: a meta-analysis of genome-wide association studies. Lancet Neurol. *18*, 1091–1102.
110. Grove, J., Ripke, S., Als, T.D., Mattheisen, M., Walters, R.K., Won, H., Pallesen, J., Agerbo, E., Andreassen, O.A., Anney, R., et al. (2019). Identification of common genetic risk variants for autism spectrum disorder. Nat. Genet. *51*, 431–444.
111. Watanabe, K., Mirkov, M.U., de Leeuw, C.A., van den Heuvel, M.P., and Posthuma, D. (2019). Genetic mapping of cell type specificity for complex traits. Nat. Commun. *10*, 3222.
112. Ting, J.T., Lee, B.R., Chong, P., Soler-Llavina, G., Cobbs, C., Koch, C., Zeng, H., and Lein, E. (2018). Preparation of acute brain slices using an optimized N-methyl-D-glucamine protective recovery method. J. Vis. Exp. https://doi.org/10.3791/53825.
113. Boudewijns, Z.S.R.M., Groen, M.R., Lodder, B., McMaster, M.T.B., Kalogreades, L., de Haan, R., Narayanan, R.T., Meredith, R.M., Mansvelder, H.D., and de Kock, C.P.J. (2013). Layer-specific high-frequency action potential spiking in the prefrontal cortex of awake rats. Front. Cell. Neurosci. *7*, 99.
114. Larkum, M.E., Nevian, T., Sandler, M., Polsky, A., and Schiller, J. (2009). Synaptic integration in tuft dendrites of layer 5 pyramidal neurons: a new unifying principle. Science *325*, 756–760.
115. García-León, J.A., García-Díaz, B., Eggermont, K., Cáceres-Palomo, L., Neyrinck, K., Madeiro da Costa, R., Dávila, J.C., Baron-Van Evercooren, A., Gutiérrez, A., and Verfaillie, C.M. (2020). Generation of oligodendrocytes and establishment of an all-human myelinating platform from human pluripotent stem cells. Nat. Protoc. *15*, 3716–3744.
116. Fernandopulle, M.S., Prestil, R., Grunseich, C., Wang, C., Gan, L., and Ward, M.E. (2018). Transcription factor-mediated differentiation of human iPSCs into neurons. Curr. Protoc. Cell Biol. *79*, e51.
117. Nehme, R., Zuccaro, E., Ghosh, S.D., Li, C., Sherwood, J.L., Pietilainen, O., Barrett, L.E., Limone, F., Worringer, K.A., Kommineni, S., et al. (2018). Combining NGN2 programming with developmental patterning generates human excitatory neurons with NMDAR-mediated synaptic transmission. Cell Rep. *23*, 2509–2523.
118. Busskamp, V., Lewis, N.E., Guye, P., Ng, A.H.M., Shipman, S.L., Byrne, S.M., Sanjana, N.E., Murn, J., Li, Y., Li, S., et al. (2014). Rapid neurogenesis through transcriptional activation in human stem cells. Mol. Syst. Biol. *10*, 760.
119. Zhang, Y., Pak, C., Han, Y., Ahlenius, H., Zhang, Z., Chanda, S., Marro, S., Patzke, C., Acuna, C., Covy, J., et al. (2013). Rapid single-step induction of functional neurons from human pluripotent stem cells. Neuron *78*, 785–798.
120. Di Giorgio, F.P., Boulting, G.L., Bobrowicz, S., and Eggan, K.C. (2008). Human embryonic stem cell-derived motor neurons are sensitive to the toxic effect of glial cells carrying an ALS-causing mutation. Cell Stem Cell *3*, 637–648.

STAR★METHODS

KEY RESOURCES TABLE

REAGENT or RESOURCE	SOURCE	IDENTIFIER
Antibodies		
Human Oligodendrocyte O4 antibody	R&D systems	Cat#MAB1326; RRID:AB_357617
Anti-MBP antibody	Millipore Sigma	Cat#AB9348; RRID:AB_11213157
Anti-NeuN antibody	Millipore Sigma	Cat#MAB377; RRID:AB_2298772
Anti-PAX6 antibody	Abcam	Cat#AB78545; RRID:AB_1566562
W0-2 primary antibody	Sigma-Aldrich	Cat#MABN10
Goat anti-Mouse IgG	Thermo Fisher	Cat#A-11004; RRID:AB_2534072
6F3D amyloid-beta antibody	DAKO	Cat#M0872; RRID:AB_2056966
AT8 p-tau antibody	Thermo Fisher	Cat#MN1020; RRID:AB_223647
Biological samples		
Human brain specimens	Kuopio University Finland	N/A
Chemicals, peptides, and recombinant proteins		
Puromycin Dihydrochloride	Thermo Fisher	Cat#A1113803
E8 Media	Thermo Fisher	Cat#A2858501
ReleSR media	Stem Cell Technologies	Cat#05872
Gibco MEM solution	Thermo Fisher	Cat#11140-050
2-mercaptoethanol	Thermo Fisher	Cat#21985023
N2 supplement	Thermo Fisher	Cat#17502048
B27 supplement	Thermo Fisher	Cat#12587010
Insulin solution	Sigma Aldrich	Cat#I9278
Retinoic acid	Sigma Aldrich	Cat#R2625
SB431542	ReproCell	Cat#04-0010-10
LDN193189	ReproCell	Cat#04-0074
Smoothened agonist	EMD Millipore	Cat#566660
Accutase	Thermo Fisher	Cat#A1110501
poly-L-ornithine	Sigma Aldrich	Cat#P3655
Laminin	Sigma Aldrich	Cat#L2020
Doxycycline	Sigma Aldrich	Cat#D9891
XAV939	ReproCell	Cat#04-00046
Neurobasal media	Gibco	Cat#21103049
BDNF	R&D systems	Cat#248-BD/CF
CTNF	R&D systems	Cat#257-33 NT/CF
GDNF	R&D systems	Cat#212-GD/CF
Triton-X	Sigma Aldrich	Cat#T9284
Prolong with NucBlue	Thermo Fisher	Cat#P36981
Matrigel	VWR	Cat#47743-716
mTesR1	StemCell Technologies	Cat#85857
Versene	Fisher Scientific	Cat#BE17-711E
RevitaCell	Thermo Fisher	Cat#A2644501
PBS	Thermo Fisher	Cat#10010049
2% low-melting point agarose	SeaPlaque, Lonza	Cat#50101
NMDA	Sigma Aldrich	Cat#M3262
NMDG-methyl-D-Glucamine	Sigma-Aldrich	Cat#M2004
KCl	Scharlau Chemicals	Cat#PO02001000
HEPES	VWR	Cat#0511

(*Continued on next page*)

Continued

REAGENT or RESOURCE	SOURCE	IDENTIFIER
NaHCO3	VWR	Cat#27778.260
NaH2PO4	VWR	Cat#28015.294
Na-Pyruvate	Fisher Scientific	Cat#BP356
Thiourea	Sigma-Aldrich	Cat#T7875
Na-Ascorbate	VWR	Cat#27688.235
MgCl2	VWR	Cat#E525
CaCl2	VWR	Cat#190464K
Glucose	VWR	Cat#101175P
Critical commercial assays		
10x Genomics v3 kit	10x Genomics	Cat#1000075
V-Plex Plus Aβ Peptide Panel 1 (6E10) ELISA kit	MesoScale Discovery	Cat#K15200G
Deposited data		
Raw and analyzed biopsy data	This paper	braincelldata.org/resource
AD snRNA-Seq dataset	Mathys et al.[3]	Synapse portal: syn18485175
AD snRNA-Seq dataset	Leng et al.[4]	Synapse portal: syn21788402
AD snRNA-Seq dataset	Lau et al.[5]	GEO: GSE157827
AD snRNA-seq dataset	Gerrits et al.[6]	GEO: GSE148822
AD snRNA-seq dataset	Zhou et al.[72]	Synapse portal: syn21125841
AD snRNA-seq dataset	Grubman et al.[73]	GEO: GSE138852
AD single soma RNA-seq dataset	Otero-Garcia et al.[7]	GEO: GSE129308
PD snRNA-seq dataset	Kamath et al.[49]	GEO: GSE178265
PD snRNA-seq dataset	Smajić et al.[50]	GEO: GSE157783
MS snRNA-seq dataset	Jäkel et al.[52]	EGA: EGAS00001003412
ASD snRNA-seq dataset	Velmeshev et al.[51]	SRA: PRJNA434002
Human snRNA-seq dataset	Li et al.[74]	PsychENCODE
Human snRNA-seq dataset	Lake et al.[75]	GEO: GSE97942
Human snRNA-seq dataset	Habib et al.[76]	Single cell portal
Human snRNA-seq dataset	Hodge et al.[77]	Allen Brain Atlas data portal
Human snRNA-seq dataset	Bakken et al.[21]	Allen Brain Atlas data portal
Mouse brain sc/sn RNA-seq dataset	Yao et al.[78]	RRID: SCR_016152
Mouse brain scRNA-seq dataset	Bhattacherjee et al.[79]	GEO: GSE124952
Mouse AD snRNA-seq dataset	Habib et al.[22]	GEO: GSE143758
Mouse AD snRNA-seq dataset	Zhou et al.[72]	GEO: GSE140511
Mouse microglia scRNA-seq dataset	Hammond et al.[80]	GEO: GSE121654
Mouse MARS-seq dataset	Keren-Shaul et al.[40]	GEO: GSE98969
Mouse microglia scRNA-seq dataset	Sierksma et al.[81]	GEO: GSE142267
Mouse microglia scRNA-seq dataset	Sala Frigerio et al.[82]	GEO: GSE127893
Mouse scRNA-seq dataset	Dulken et al.[83]	Bioproject: PRJNA450425
Mouse scRNA-seq dataset	Masuda et al.[84]	GEO: GSE120747
Mouse scRNA-seq dataset	Zywitza et al.[85]	GEO: GSE111527
Mouse scRNA-seq dataset	Chen et al.[86]	GEO: GSE87544
Human reference genome NCBI build 37, GRCh37 (hg19)	Genome Reference Consortium	GRCh37 (hg19)
Experimental models: Cell lines		
H1 stem cell line	WiCell	H1
Recombinant DNA		
TALEN-L plasmid	Addgene	Cat#59025
TALEN-R plasmid	Addgene	Cat#59026

(*Continued on next page*)

Continued		
REAGENT or RESOURCE	SOURCE	IDENTIFIER
Bcl-XL plasmid	Addgene	Cat#8790
Software and algorithms		
FUMA	Watanabe et al.[87]	https://fuma.ctglab.nl
MAGMA v1.08	de Leeuw et al.[43]	https://ctg.cncr.nl/software/magma
DropSeqTools	Macosko et al.[88]	https://github.com/broadinstitute/Drop-seq
CellProfiler4.2.5	Stirling et al.[89]	https://cellprofiler.org/
Discovery Workbench 4.0	Meso Scale Diagnostics	https://www.mesoscale.com/en/products_and_services/software
R v4.0.4	R core team	https://www.R-project.org/
Neuroexplorer	Nex Technologies	https://www.neuroexplorer.com
MATLAB	MathWorks	https://www.mathworks.com/products/matlab.html
MCS Experimenter v2.15	MultiChannel Systems	https://www.multichannelsystems.com/software/multi-channel-experimenter

RESOURCE AVAILABILITY

Lead contact

Inquiries about further information and requests for resources and reagents should be directed to the Lead Contact, Evan Z. Macosko (emacosko@broadinstitute.org).

Materials availability

This study did not generate new unique reagents.

Data and code availability

- All generated snRNA-seq data and the results of our integrative analysis of 28 single-cell/nucleus studies are publicly available at: https://braincelldata.org/resource. This includes sample annotations related to the dataset source (36 datasets across 28 studies), cell identifiers (e.g., cell barcodes), quality metrics, and cell type annotations from integrative analysis. We have also included functionality to perform several analyses in a fast and efficient way, including: examination of the integration solutions, performing marker analysis across all of the datasets, and exploring differentially expressed genes.
- The code used to generate results presented in this manuscript are publicly available as a Terra workspace (https://app.terra.bio/#workspaces/fbrihuman/sconline_integrative_analysis).
- Any additional information required to reanalyze the data reported in this paper is available from the lead contact upon request.

EXPERIMENTAL MODEL AND STUDY PARTICIPANT DETAILS

Primary biopsy cohort

The cohort used for snRNA-seq analysis included biopsy specimens from 52 patients that were evaluated for adult hydrocephalus with NPH symptoms at the Kuopio University Hospital. They included 47 with idiopathic normal pressure hydrocephalus, 3 with previously unrecognized congenital hydrocephalus and 2 with acquired hydrocephalus. The 52 individuals included 30 males and 22 females with a mean age of 73 years (standard deviation: 7 years), all of Finnish ancestry. Assessment of biopsy samples by a neuropathologist under light microscopy identified 19 with Aβ plaques (Aβ+), eight with both Aβ plaques and phosphorylated tau pathology (Aβ+Tau+), and 25 biopsies that had neither histopathology. Patients were consented for retrieval of brain biopsies during ventriculoperitoneal shunt placement for treatment of their symptomatic adult hydrocephalus. The biopsy procedure was approved by the Research Ethics Committee of the Northern Savo Hospital District (decision No. 276/13.02.00/2016). See Table S1 for more details.

Validation cohort

The validation cohort for the electrophysiological experiments included biopsy specimens from 26 individuals. Similar to the main biopsy cohort, these individuals were evaluated for an adult hydrocephalus with NPH symptoms at the Kuopio University Hospital. The 26 individuals included 14 males and 12 females with a mean age of 74 years (standard deviation: 6 years). Assessment of biopsy samples by a neuropathologist under light microscopy identified 16 out of 26 with Aβ pathology. Patients were consented for retrieval of brain biopsies during ventriculoperitoneal shunt placement for treatment of their symptomatic adult hydrocephalus. The biopsy procedure was approved by the Research Ethics Committee of the Northern Savo Hospital District (decision No. 276/13.02.00/2016). See Table S1 for more details.

Cell lines

The H1 embryonic stem cell line (male sex) was used to derive iExNs and iOligos for measurement of amyloid-beta peptides. Cell lines were maintained under standard incubator conditions, at 37°C and 5% CO2 and passaged when approaching confluence using methods described below. The H1 stem cell line was frozen down for future storage and re-plating in liquid nitrogen. The H1 cell line was authenticated for identity through concordance analyses from genotypes sequenced using the Infinium GSA-24 v3.0 in house compared with a reference genotype from WiCell. Genotypes are ascertained every few cell line expansions to confirm donor identity.

METHOD DETAILS

Procurement of frontal cortex brain biopsies

Biopsies were taken at the site where the shunt would penetrate the brain. Three cylindrical biopsies were taken approximately 2mm in diameter and 3-10mm in length using a disposable Temno Evolution TT146 (Merit Medical Systems) biopsy tool. The insertion point of the catheter was approximately 3 cm from the midline and anterior to the coronal suture.[90] Biopsies were immediately frozen with liquid nitrogen and stored at -80°C. One biopsy was sent for histopathological staining using the 6F3D and AT8 antibodies and evaluated by a neuropathologist for presence of Aβ plaques and tau tangles via light microscopy.[91] Biopsy Aβ plaques burden was further assessed semiquantitatively by a neuropathologist (T.R.) under light microscopy and assigned to mild (1), moderate (2), or severe amyloid burden (3) as described previously.[92] Our initial cohort included 58 individuals. We excluded one individual with tau-only pathology and another patient with a history of psychosis. We excluded four additional individuals (2 Aβ-free and 2 Aβ+) that, upon microscopic inspection of Nissl stained cryosections (see the biopsy tissue quality scoring methods), displayed decidedly poor tissue quality and a very high ratio of white matter to cortical matter. All of these excluded biopsies were more than 85% white matter tracts with the diminished cortical regions showing dysmorphic neuronal profiles.

Neuroanatomical localization of biopsy site

The stereotactic position (distances in millimeters) was measured from anatomically linked planes (transverse, sagittal, coronal) in a multiplanar reconstruction (MPR) produced from the postoperative CT/MRI DICOM image. After planar alignment (transverse and sagittal planes to the midline, and coronal plane in a 90-degree angle to the planum sphenoidale), the biopsy location was determined to be at proximal catheter's cortex entry site at the catheter's midline. Following distances were measured: In the transverse plane from the midline to the biopsy location (x). In the sagittal plane from the frontal bone's internal cortex to the biopsy location's coronal axis (at 90-degree angle) (y). In the sagittal plane, distance from the planum sphenoidale to the biopsy location's transverse axis (at 90-degree angle) (z). EBRAINS Siibra-explorer was used to map and visualize each biopsy position.[93–95]

Biopsy tissue quality scoring

To ascertain tissue quality measurements (range from 1-10), we performed Nissl staining followed by semi-quantitative scoring of each biopsy slide image. For Nissl staining, briefly, fresh frozen tissue was thermally equilibrated to -20°C in a cryostat (Leica CM3050S) for 20 minutes. Tissue was mounted onto a cryostat chuck with Optimal Cutting Temperature compound (O.C.T. compound), aligned at a 5° cutting angle, and sectioned at 10 μm in thickness per tissue slice. Using a Superfrost plus slide that has been pre-cooled to -20°C, the tissue section was collected by carefully placing it and gently flattening it with the brush on top of the slide. Subsequently, slides were stained with 0.1% Cresyl Violet acetate in DiH_2O, destained with ethanol, and 100% Xylene for 5 minutes. Slides were mounted by adding 2-3 drops of Permount around the tissue and coverslipped. Images were subsequently collected using a Keyence BZ-X810 series All-in-one Fluorescence microscope. With BZ-X800 viewer software, each stained slide was imaged on the Brightfield/Phase contrast channel using a 20X objective. The stained region of interest was selected by specifying the XY positions of the tissue outer edges and adjusting the Z-stack function to auto-focus prior to each image capture. The stitching of captured image series was made with BZ-X800 analyzer software. The images are exported as Big TIFF files and edited for cropping, contrast, and brightness with Photoshop software.

Measurement of iNPH grading scale and clinical diagnosis

Severity of idiopathic normal pressure hydrocephalus (iNPH) symptoms was evaluated using the iNPH grading scale (iNPHGS),[96] a clinician-rated scale that aims to assess the hallmark triad of the disease. Inversely correlated with the severity of the disease, the 12-point iNPHGS has been shown to be clinically meaningful down to a single point.[96] Longitudinal clinical information on our cohort of 52 individuals was obtained by following up patients until death (n=23) or April 2023 with a median of 5 years.

Generation of single-nuclei suspensions from frozen brain biopsies

Fresh-frozen brain biopsy tissue was cryosectioned at -15 to -20°C into 60-micron sections. Following microdissection, samples were placed on dry ice until nuclei isolation. To each cryosectioned sample, 1mL of Extraction Buffer (ExB) was added into a 1.5mL Eppendorf tube. Samples were briefly triturated before being placed in a six-well plate. Samples were then triturated 20 times with the ExB, every 2 minutes, until no large chunks of tissue were observed in each well. After the last trituration, samples were

diluted with 45-50mL of wash buffer in a 50mL Falcon tube, and then split into four 13-15mL solutions in 50mL Falcon tubes. The diluted samples were then spun at 500g for 10 minutes at 4°C (pre-cooled) in a swing bucket benchtop centrifuge.

After centrifugation, a visible nuclei pellet was observed. Samples were then removed very gently from the centrifuge, and placed in an ice bucket. The supernatant was aspirated until there was barely any liquid observed on top of the pellet (50-100μL of liquid left). To aspirate without disturbing the pellet, a serological pipette was first used till about 1mL was remaining, followed by serial aspiration with a P2000 and P200 pipette.

The pellets were then resuspended in 250μL of wash buffer (WB), mixed thoroughly by trituration and placed in an Eppendorf 1.5mL tube.

Single-nucleus and single-cell RNA-sequencing and read pre-processing

For all single-nuclei experiments, the 10X Genomics (v3) kit was used according to the manufacturer's protocol recommendations. Library preparation was performed according to the manufacturer's recommendation. Libraries were pooled and sequenced on either a NovaSeq S2 or S4.

Sequencing reads from human brain biopsy experiments were demultiplexed and aligned to the hg19 reference using DropSeqTools (https://github.com/broadinstitute/Drop-seq) with the default settings. To reduce background noise from ambient RNA and potential UMI barcode swaps, we used Cellbender remove-background v2[97] with the default applied settings to all libraries. The Cellbender-corrected reads were used for downstream variable gene selection, dimensionality reduction, clustering, and differential expression. Cellbender was also used to distinguish cells from empty droplets.

Initial clustering of the biopsy cohort

Pre-processed Cellbender-corrected digital expression matrices were loaded into R per library as a digital gene expression matrix. All matrices were combined per individual and an initial variable gene selection was performed. A low-dimensional embedding was generated via rliger v1.0 at a k = 45 and lambda = 5. Following integrative non-negative matrix factorization,[18] a shared nearest neighbors graph was generated and individual nuclei profiles were clustered according to the SLM (smart local moving) algorithm to identify broad cell classes. We used a recent large-scale survey of postmortem human brain[21] to identify cell class markers and merged each cluster into one of eight cell classes (excitatory neurons, inhibitory neurons, astrocytes, microglia/macrophages, oligodendrocytes, oligodendrocyte precursor cells, endothelial cells/pericytes, and peripheral blood mononuclear cells (PBMCs)). PBMCs were excluded from downstream analysis.

For each cell class, individual nuclei were subsetted and the above clustering process was repeated to identify individual cell types. Marker genes were identified for neuronal populations based on a large-scale survey of neurons in the human neocortex.[21] Further, a recent survey of microglia/macrophage in the murine brain was used to identify cell type markers for microglia and macrophages.[80] For other non-neuronal types, we performed the Wilcoxon rank-sum test on SLM-defined cell clusters to find markers and thereby determine cell type annotations. We removed doublets identified as clusters that expressed markers of more than one cell class population. We also removed clusters whose markers contained high numbers of mitochondrial genes or heat shock related proteins.

Integrative analysis of the biopsy dataset with postmortem studies

We collected and uniformly processed all publicly available metadata on each dataset including the donor information (e.g., age, sex, diagnosis), sample information (e.g., brain region, sequencing protocol, batch structure), cell type identities, and quality metrics. All gene identifiers were mapped to Ensembl gene id. For mouse datasets, we further mapped Ensembl gene ids to their human orthologs.[98] However, we did retain non-orthologous mouse genes for normalization. We calculated the following quality metrics for every cell in each dataset: number of unique genes (nGene) and number of unique molecular identifiers (nUMI), percentage of mitochondrial genes (MT%), percentage of ribosomal genes (Ribo%), percentage of non-coding lncRNAs (lncRNA%), and percentage of dissociation-related artifacts%.[20] We used nGene and MT% quality metrics as our initial criteria to select cells for our integrative analyses and used the other quality metrics to identify and remove low quality cell clusters from the integrative analysis results. We retained cells with nGene >500 and MT% <5. For microglia cells, we used nGene >200 for two studies[4,40] to compensate for the lower number of unique genes compared to other cell types. We further used the nGene >200 threshold for all cell classes in Mathys et al. dataset.[3] Finally, we removed donors with less than 50 cells within each cell class. Our integrative analyses across the seven cell classes included a total of 2,406,980 high quality cell profiles across 36 datasets from 28 studies on humans and mice. Distributions of the quality metrics are included in Figures 1C and S1E. See data and code availability section for information about availability of the integrative analysis.

We performed our integrative analysis of each cell class individually to maximize the accuracy of cell state mapping across datasets. The seven major cell classes were: excitatory neurons (ExN), inhibitory neurons (InN), astrocytes (Astro), microglia/macrophages (Micro), oligodendrocytes (Oligo), Oligodendrocyte progenitor cells (OPC), and endothelial/pericyte cells (Endo). For Inhibitory and excitatory neurons, we limited our analysis to cortex brain region. However, glial cells were represented from across the brain regions. Table S1 summarizes the datasets that are included in integrative analysis of each of the seven cell classes. As outlined below, we developed a multi-step framework to efficiently handle substantial biological and technical variation that exists among the single-cell and single-nucleus datasets.

Selecting highly variable genes

We reasoned that the influence of batch effects on the cell embedding space would be minimized by selection of genes that recurrently show high variability across the human and mouse datasets. To achieve this, we implemented the following method: 1) Select the top 2000 variable genes within each donor of each dataset by the vst method in Seurat.[99] 2) Weight the selected genes in each donor so that the sum of the weights for each dataset add up to one. 3) Calculate an aggregate score for each gene by summing up their weighted scores. This procedure aims to minimize the participation of genes that show between dataset variability (hence likely influenced by batch effects) in the follow up analysis of cell embedding construction and clustering.

Principal component analysis

To remove donor-specific batch effects (e.g., due to pre and post-mortem effects, sample preparation, and sequencing settings), we performed scaling (i.e., mean of zero and unit variance) of transcriptome data per gene and per donor and used this scaled data for principal component analysis. Comparison of different integrative solutions indicated the better quality after removal of donor specific effects. For all seven cell class analyses, we used the top 30 principal components, weighted by their variance explained.

Batch effect removal

We used Harmony v1.0[100] to remove batch effects from the PCs with donor id and organism specified as the main source of batch effects. The default theta and lambda parameters were used for all analyses, except for the Endo cells with the theta parameter of four.

Assessing the quality integration solutions

To assess the quality of the results, we developed multiple "cluster-free" quality metrics enabling us to perform a systematic and unbiased comparison of the solutions that is independent of the clustering method. These metrics can be grouped into three main categories. First, we required a uniform distribution of the datasets in the Uniform Manifold Approximation and Projection (UMAP) space. In addition to visual inspection, we developed a method that allowed us to do a quantitative evaluation of dataset distributions. Briefly, each of the two UMAP coordinates are split to 100 units, providing 10,000 bins. Within each bin a hypergeometric test is performed to assess whether or not cells from a specific dataset are over-represented. This analysis is performed for each dataset from each integrative solution (the related R functions and visualizations are provided at https://braincelldata.org/resource). Second, we examined whether cells expressing known cortical cell type markers are aligned with each other across datasets and organisms. To systematically test this, we repurposed the commonly used feature plot visualizations to represent donors instead of individual cells, thereby bypassing the effect of sample size variation between donors and datasets. Finally, we assessed if the initial clustering structure of each dataset is preserved in the aligned space. For this analysis, we used the reported clustering structure for each of the datasets individually. We also constructed confusion matrices to compare the cluster annotations between datasets (see the linked website for more details).

Cluster quality analysis

On each cell class integrative analysis we performed Leiden clustering using the Seurat package[99] with clustering resolutions of 0.6 or 0.8. We next used our calculated cell-based quality metrics (nGene, nUMI, MT%, Ribo%, lncRNA%, and %expression of dissociation-related artifacts) to identify and remove low quality clusters. We also performed marker analysis of each cluster per each dataset using FindAllMarkers() function in Seurat to identify and remove doublet clusters.

Uniform annotation of the datasets

We modified a previously developed random walk algorithm[101] to transfer cell type annotations from the biopsy dataset to each of 35 datasets (27 studies) in the aligned space, thereby uniformly annotating all datasets with cluster labels from the biopsy cohort. We next checked the consistency of cell type proportions among datasets and expression of marker genes across datasets and clusters (Table S2; See the linked website for more details).

Cell type marker analysis

Marker genes were identified in each dataset by running the 'FindAllMarkers' function in Seurat.[99] Significant genes (FDR-adjusted p value < 0.1) with min.diff.pct of 0.1 were considered as markers. The heatmap in Figure 4A based on a select number of microglia markers based on the existing knowledge on microglia states and function. The full organized marker results are provided in Table S2.

To assess an overlap between cell state markers and DE genes in the microglia analysis (Figure 4D), we retained the top 100 upregulated markers (FDR-adjusted p value < 0.01; sorted by p value) that were markers with log fold-change (logFC) >0 in less than a third of the cell states. This additional criterion was added to avoid spurious overlap of markers in non-homeostatic microglia that were driven by the large size of the homeostatic microglia.

Differential abundance analysis

In our integrative analysis, a major analytic challenge was the wide variation in cell class compositions among the analyzed datasets. As an illustration, both of human PD datasets, one of human AD datasets, and all of mouse AD datasets included only glial cells and not neuronal cells from cortex. To address this, we conducted our meta-analysis of cell type proportional changes within each cell class separately. For our meta-analysis of early AD pathology, we included three out of 6 AD postmortem cohorts from the frontal lobe (more specifically prefrontal cortex or superior frontal gyrus).[3,4,6] We excluded one cohort[72] due to overlap of individuals with another included cohort,[3] and two that lacked sufficient numbers of early AD stage subjects.[5,7] We further included two PD postmortem datasets,[49,50] one ASD dataset[51] and one MS dataset[52] as contrast groups in our analyses.

We used a logistic mixed-effect model[102] to identify differentially abundant cell populations in each dataset separately (Table S3). For all human datasets, we included sex as a fixed effect, and individual as a random effect in the model. We then tested the significance of association between the status with the clusters using a Wald test. For assessing cell type abundance associations with iNPH grading scales, we modified the method to allow for continuous independent variables, while preserving the Wald test for assigning significance.

We performed a meta-analysis of cell type abundance results across four cohorts with designations for earlier and later AD stages: (1) the biopsy cohort (Aβ+ as early and Aβ+Tau+ as late; all cell classes), (2) Mathys et al. (Braak III-IV as early and Braak V-VI as late; all cell classes except endothelial cells), (3) Leng et al. (Braak III-IV as early and Braak V-VI as late; all cell classes) and (4) Gerrits et al. (CtrlPlus as early and AD as late). The p values from individual analyses were combined together via the Stouffer's method, with an additional consideration of the directionality of the change as determined via the odds ratio assessment from the Wald test. All Stouffer's p values were subsequently corrected for multiple hypothesis testing via the Benjamini-Hochberg correction.

To determine the relative cellular abundance changes at the cell class level we generated p values by comparing proportions of the seven cell classes by a Wilcoxon rank-sum test. Meta-analysis p values (and Z scores) were generated using Stouffer's method, taking into account the directionality of the abundance change (Figure S2F).

For mouse datasets, we used Fisher's exact test to examine expansion and loss of different microglia cell types and states (Table S3). The p values were subsequently corrected for multiple hypothesis testing using the Benjamini-Hochberg procedure. For visualization purposes, Z scores were calculated by transformation of the p values and signed by the directionality of the log odds ratio.

Differential gene expression analysis

We employed a pseudocell strategy coupled with mixed linear models and jack-knifing to robustly identify differentially expressed genes. To construct pseudocells, we aggregated the raw UMI count of, on average, every 30 cells per subject and cell type. We constructed one pseudocell for cell types that had between 15 to 45 cells in a donor and excluded cell types that had less than 15 cells. Pseudocell-based analysis reduces the impact of dropout and technical variability, while ameliorating low statistical power and high variation in sample size issues attributed to the pseudobulk approaches.[103] We used the Limma Trend[104] approach with robust moderated t-statistic to identify DE genes within each cell class with sex, cell type, $\log_2$(pseudocell MT%) and $\log_2$(pseudocell nUMI) as covariates and subject id as a random effect. Cell type annotation was included as a covariate to account for the cell type-specific baseline expression of the genes and therefore to ameliorate the impact of cell type proportion on the DE patterns.

We further performed jack-knife resampling at two levels to identify robust DE genes that are shared among the majority of individuals. First, iterating on each of the 52 individuals in the biopsy cohort, we excluded one subject from the analysis of each cell class and then re-calculated the DE statistic for the remaining 51 individuals, retaining the maximum p value (i.e., the least significant p value) achieved for each gene. An FDR-adjusted jack-knife p value was next calculated for genes with FDR-adjusted p value < 0.1 in the main analysis using the Benjamini-Hochberg correction. Second, iterating 50 times, we randomly sampled 50% of cohort subjects (balanced by their pathological status) and re-calculated the logFC patterns. A consistency score was defined for each gene as the fraction of iterations in which the jack-knifed logFCs were consistent with the logFC pattern from the full cohort of 52 individuals (i.e., up- or down-regulated in both). Genes with FDR-adjusted jack-knife p value < 0.01 and jack-knifed consistency score ≥ 0.9 were deemed as significant. Comparison of the DE patterns with a pseudobulk approach using LimmaTrend indicated highly consistent (>99%) logFC patterns between the pseudobulk and our pseudocell strategy for the DE genes. We also found majority of identified DE gens by pseudocell approach remain significant (median >72% per cell class; pseudobulk FDR-adjusted p value < 0.1) in the pseudobulk approach, while the identified DE genes by our pseudocell approach show much less sensitivity to variation in cohort size (data not shown).

To compare the DE genes between Aβ+ and Aβ+Tau+ individuals (Figure 2D), we performed a paired t-test based on values from below equation:

$$sign(logFC(A\beta +) * logFC(A\beta + Tau +)) * sign(logFC(A\beta + Tau +)) * [logFC(A\beta + Tau +) - logFC(A\beta +)]$$

This equation will be positive only if the logFC from both Aβ+ and Aβ+Tau+ are in the same direction (i.e., gene is up or down regulated in both conditions) and are stronger in Aβ+Tau+ and negative otherwise. We excluded from this analysis cell types with less than 20 DE genes in either Aβ+ and Aβ+Tau+ conditions as they usually were small and their fold change patterns were not reliable. We used a paired t-test to determine if the outputs of this function are randomly distributed around zero or are biased towards positive (i.e., consistent but stronger logFC in Aβ+Tau+) or negative (i.e., discordant or stronger in Aβ+) values.

Gene set enrichment analysis

DE genes were filtered to protein-coding based on the gene biotype information from the 'EnsDb.Hsapiens.v86' package in R Bioconductor. Genes were next ordered based on their t-statistic from LimmaTrend mixed linear models. Curated GO Biological Process, KEGG and Reactome gene sets were retrieved from the EnrichR portal.[105] To identify enriched pathways, we ran the fGSEA package[106] v1.16.0 with default setting while limiting the geneset sizes between 15 and 250 genes. For each cell class and cell type analysis, protein-coding genes expressed in more than one percent of cells in the corresponding group were used as background.

Correlating cell-type-proportional changes to transcriptome responses across cell types

To identify correlation between cell type abundances and transcriptional phenotypes, we used a logistic mixed-effect model.[102] Specifically, we constructed a meta-gene (referred to as DE signature in the main text) from the top 300 upregulated protein-coding genes (sorted by their jack-knifed p value) in each individual cell by aggregating their corresponding UMI counts, as proposed before.[107] The meta-gene was next normalized over the total nUMI count of the cells and standardized to have a mean of zero and variance of one across cells from all subjects in our cohort. We then binarized cells as active or inactive for a meta gene based on a standardized score threshold of 2. In our analyses we required presence of at least two subjects with more than 3% transcriptionally active cells in each cell type and status category. For cell types that do not meet this criterion we set the association p value to one to indicate transcriptional changes in the corresponding cell type are not associated with the interested cell type fractional variation. Finally, we fit a logistic mixed-effect model on the binarized scores to examine their association with the normalized cell type proportional changes with sex as a covariate and subject as a random effect. The cell type proportions were normalized by applying an empirical cumulative estimation using the ecdf() function in R. We used cell-class level DE genes to construct meta-genes since: 1) cell class level DE genes were highly conserved within cell types (Figure S2G); 2) DE genes were not driven by the variation in the cell counts of the cell types. As summarized below, we performed robustness analysis and alternative meta-gene construction schemes to further confirm the observed associations.

First, to assess the robustness of the results, we tested the sensitivity of the results to the presence of technical variation in cell gene counts by, iterating 30 times, adding Poisson noise to the transcriptome data of each individual cell before calculation of the meta-gene expressions (Figure S3B). In addition, iterating 30 times we randomly down sampled the cell types to examine the association of the cell type sizes on the results (Figure S3C).

Second, as an alternative analysis method to support our findings (Figure S3D), we constructed meta-genes through principal component analysis of the normalized and scaled expression of the top 300 upregulated protein-coding genes (sorted based on jack-knifed p values). Similar to the WGCNA approach,[108] the first principal component was chosen as the meta-gene. The meta-gene scores were then binarized as above and the association with cell type proportional changes were examined using a logistic mixed-effects model similar to above.

Heritability enrichment of differentially expressed genes with MAGMA

We used MAGMA[43] to determine the degree of enrichment of common variant risk in the list of differentially expressed genes across cell types. We first downloaded the summary statistics from a recent common variant meta-analysis of AD and related dementias,[36] PD,[109] and ASD.[110] Using the online FUMA tool,[111] we generated Z scores for each gene, corresponding to the approximate degree of association between the gene and AD (SNP2GENE function). To determine gene sets for each cell class, we took the top 200 differentially expressed genes between biopsy samples with AD pathology versus those samples without, ordered by t-statistic at a significance value of $p < 0.2$ (to ensure enough genes were being captured per gene set). Significance values for the gene set of interest were calculated via MAGMA, wherein a regression is fit to determine whether those genes with membership for that set have a significant enrichment for heritable risk of the trait of interest.

Brain slice preparation for electrophysiological experiments

Brain biopsies were collected from the right frontal lobe from a standard insertion site (mid pupillary line, 2 mm anterior to the coronal suture representing Brodmann area 8) before insertion of the intraventricular catheter for cerebro-spinal fluid (CSF) shunt as described previously.[13,90] A pyramid/rectangular shaped right lobe cortical biopsy of around 3 mm in edge was extracted by sharp cut of a knife and gently lifted and placed into a sterile 50mL falcon tube containing ice-cold, sterile filtered, N-methyl-D-glucamine (NMDG)-based artificial CSF solution (aCSF; see below for composition).[112] The brain biopsies were brought to the neurophysiology laboratory within 15 to 20 minutes from excision. Brain biopsies were gently cleaned of any debris or blood clots by careful trituration with a large bore fire polished glass Pasteur pipette, photographed for sample size documentation and were then embedded in 2% low melting point agarose (SeaPlaque, Lonza USA) and sliced (350 μm) using a vibratome (Campden Instruments, model 7000 smz) in chilled (2-4 °C), fully carbogenated (95%/5%, O_2/CO_2) aCSF of the following composition (in mM): 92 NMDG-methyl-D-Glucamine, 2.5 KCl, 20 HEPES, 25 $NaHCO_3$, 1.25 NaH_2PO_4, 3 Na-Pyruvate, 2 Thiourea, 5 Na-Ascorbate, 7 $MgCl_2$, 0.5 $CaCl_2$, 25 Glucose (pH adjusted to 7.3 with HCl 10 M). We routinely discarded the first and last slice (extremities of sample) obtained and only two mid-sample mini slices (total area of 6-10 mm^2) from each biopsy were included in our study for functional examination. After cutting, slices were photographed once again and were then placed in a custom-made chamber and allowed first to recover at 34 °C for 45 minutes in the recording solution (see below for composition, supplemented with 3 mM Na-Pyruvate, 2 mM Thiourea and 5 mM Na-Ascorbate) and then for another 60 minutes in the same solution at room temperature (20-22°C) before use for electrophysiology.

3D-multielectrode array electrophysiology

A single slice (350 μm) was transferred and secured with a slice anchor in the chamber of a 60-3D-multielectrode recording array (3D-MEA, Multichannel Systems [MCS]) with an 8x8 configuration of pyramidal electrodes bearing titanium nitride (TiN) tips (impedance 150-300 KOhm) and silicon nitride isolation. Pyramidal electrodes had a height of 100 μm but were conducting only on top 20 μm of the tip which measured 12 μm in base. Recordings were made with a MEA2100-Mini headstage (MCS, Germany) Slices were continuously perfused at a rate of 3-3.5 mL/min with a recording solution of the following composition (in mM): 120 NaCl, 2.5 KCl, 25

$NaHCO_3$, 1.25 NaH_2PO_4, 2 $CaCl_2$, 1 $MgCl_2$, 25 Glucose. Slices were allowed at least 30 minutes of settling time in the MEA chamber before any recordings or pharmacology was attempted. Drugs (NMDA, 200 μM for 2 minutes, Sigma-Aldrich) were bath applied by continuous perfusion via a peristaltic pump. Electrophysiological data were band passed between 1 and 3500Hz (second order Butterworth filter) and were captured at 20 KHz via MCS-IFB 3.0 multiboot (MCS, Germany) to a personal computer, displayed in MCS Experimenter software (version 2.15) and stored to disk for further analysis.

3D-MEA data analysis

NPH brain biopsies were selected for neurophysiological analysis after careful consideration of experimental notes, biopsy documentation images at the time of recording & Nissl staining to ascertain the preservation of pia to L4-L5 cortical layers. Multielectrode recording data files (.msrd) were imported in Neuroexplorer (Nex Technologies, US) and opened in Neuroexplorer (Nex Technologies) or MATLAB (The MathWorks) for filtering, down-sampling, measurement routines and analysis with custom scripts (python, MATLAB). Multichannel signals were analyzed for spike activity based on their cortical depth (L2/3: 300-1250 μm; L5: >=1500 μm;). Spike detection of multiunit activity (MUA) was performed from drug responding, channels of interest (COIs). Reference channel noise was subtracted from each COI before applying a 300-3500Hz band-pass filter (3rd order, Butterworth) to the raw signal followed by a spike detection threshold set at -5.5 times the standard deviation (SD) of the baseline of each COI. Electrodes qualified for analysis if they responded to NMDA drug superfusion with an increase in firing (excitation) consisting of a minimum of two consecutive 10s binned frequency peaks above 0.1Hz and a mean firing rate during NMDA application of more than 0.05 Hz. Extracted spike timestamps were stored in a file and were used to compute interspike intervals (ISI) & spike bursting characteristics for each COI during pharmacological experiments with NMDA. For burst detection, we used an interval-based algorithm to detect and quantify the characteristics of bursting induced by NMDA superfusion. We defined a cortical burst by a minimum of two spikes occurring within 10 ms of each other (minimum burst start with instantaneous doublet frequency of > 100 Hz)[113,114] with burst terminating only if the forthcoming spike occurred more than 20 ms after the last (termination instantaneous frequency of < 50Hz), while any two consecutive bursts had to be separated by a minimum of 25 ms from each other (minimum interburst interval).

Histological determinations and immunohistochemistry

A single, 350 μm, biopsy slice (3D-60MEA recorded) was fixed in fresh 4% PFA for 24-72 hours at 4°C and then stored in Phosphate Buffer (PB) containing 30% sucrose for 24 hours at 4°C for cryoprotection. Slices were then resliced into 20 μm sections at -20°C using a cryostat (Leica CM1950, Leica Biosystems, Germany) and were collected on frost slides for 6-amyloid staining. We used a standard citrate buffer antigen retrieval protocol (with 10 mM sodium citrate) prior to overnight incubation of slices with W0-2 primary antibody (MABN10, Millipore, dilution 1:1000, at room temperature) followed by a two hour incubation with an anti-mouse fluorescent secondary antibody (Alexa Fluor Goat-anti-mouse 568, A11004, Thermo Fischer Scientific, dilution 1:500) for 6-amyloid detection. NPH biopsy slices were imaged with LEICA thunder imager 3D tissue slide scanner (Cell and Tissue Imaging Unit, UEF) and the quantification of 6-amyloid burden was conducted in ImageJ. Regions of interest (ROIs) were drawn to outline the sample sections and 6-amyloid burden was quantified by measuring the fluorescence intensity and area coverage fraction (intensity per mm^2) of the WO2 staining inside each ROIs. Acquired images were first turned into 8-bit images, thresholded to minimum value of 30 and normalized to a maximum value of 120. Following the quantification of Aβ burden, the 16 Aβ+ biopsy specimens were divided into two equal-sized groups. Eight specimens were categorized as Low Aβ+, while the remaining eight were classified as High Aβ+.

Generation of a doxycycline-inducible *SOX10* H1 stem cell line

We adapted a recently-published protocol to produce mature oligodendrocytes from the H1 embryonic stem cell precursors cell line.[115] First, we isolated and incorporated a *SOX10* transcription factor (Addgene #115242) into the backbone of a doxycycline-inducible cassette (Addgene #105840) to generate pBR01.

H1 ESCs were plated in Matrigel (cat. #47743-716)-coated (30-minute incubation at 37°C prior to cell plating) plates in mTesR1 (cat. #85857) with supplements (ESC media, StemCell Technologies cat. #85857) and RevitaCell (cat. #A2644501). After plating, we performed daily media changes with ESC media without RevitaCell until plates were approximately 80% confluent with compact colonies. For routine passaging, ESCs were washed 1X with PBS (cat. #10010049) and incubated in Versene (cat. #BE17-711E) for 5 mins at room temperature, after which Versene was gently aspirated from the plate and replaced with ESC media. ESCs were gently dissociated into a cell suspension using a manual cell scraper and transferred as small colonies to a fresh Matrigel-coated plate at a 1:20 dilution. In order to generate a doxycycline-inducible *SOX10* cell line, we performed TALEN-based integration as has been previously described.[116] Briefly, we electroporated (1050V, 50 ms pulse, two pulses total) 1 million ESCs with 4 μg pBR01, 2 μg TALEN-L (Addgene #59025), 2 μg TALEN-R (Addgene #59026), and 0.4 μg Bcl-XL (Addgene #8790) plasmids using a Neon Transfection System Pipette Station (Thermo Fisher). After 96 hours, cells were incubated with 2 μg/mL puromycin (cat. #A1113803) for 72 hours. After puromycin selection, polyclonal ESCs were expanded and stored in liquid nitrogen at 10^6 cells/mL in 10% DMSO + mTesR1.

Oligodendrocyte differentiation of ESCs

To differentiate the resulting cell line into mature oligodendrocyte lineage cells, we adapted the Garcia-Leon protocol with minor modifications.[115] Briefly, we used the H1 embryonic stem cell line with the integrated *SOX10* cassette to generate neural progenitor cells which were subsequently differentiated into mature oligodendrocytes. Vials containing 1 million ESC precursors were thawed

and plated into one well of a Matrigel-coated 6-well plate, supplementing the cells with RevitaCell to increase vitality. These cells were then allowed to grow to confluence with supplementation of 1mL E8 media (cat. #A2858501). Confluent cells were subsequently split with the following procedure. First, cells were washed with 1mL of Dulbecco's PBS per well. Then, cells were subsequently treated with 1mL of ReleSR (cat. #05872) incubated at 37°C for five minutes. Cells were then spun down and split at a ratio of 1:14 into Matrigel-coated 6-well plates and grown in 1mL of E8 media (cat. #A2858501) supplemented with 1x RevitaCell solution. The cells were transitioned to mTeSR1 media by replacing with a 1:1 E8 to mTeSR1 solution on the first day, 75% mTeSR1 with 25% E8 on the second day, and a full 1mL of 100% mTeSR1 on the third day. Cells were then allowed to grow to confluence before being split again with 1mL ReleSR as above. The cells were replated onto 6-well matrigel-coated plates, supplemented with RevitaCell. An N2B27 media was made by mixing non-essential amino acid MEM (cat. #11140-050), 2-mercaptoethanol (cat. #21985023), N2 (cat. #17502048) and B27 (cat. #12587010) to 1× concentration plus insulin (cat. #I9278) at 25 μg/mL final concentration to Dulbecco's modified essential media. The cells were then grown in 2 mL of the pre-made N2B27 medium supplemented with 0.1 μM retinoic acid (RA, cat. #R2625), 10 μM SB431542 (cat. #04-0010-10) and 1 μM LDN193189 (cat. #04-0074) for five days and an additional two days with 10 μM of smoothened agonist (SAG, cat. #566660).

After cells achieved confluence, they were passaged using a pre-warmed 1mL aliquot of Accutase (cat. #A1110501) for 1-2 minutes. The cells were seeded onto 6-well plates coated with poly-l-ornithine (cat. #P3655) and laminin (cat. #L2020-1MG)-coated plates at a density of 10,000 cells per square centimeter. The cells were fed a differentiation medium supplemented with 2 μg/mL of doxycycline (cat. #D9891-10G) to induce expression of *SOX10* and allowed to grow for 10 days, at which time they are mature.

Neuronal differentiation of ESCs

Neuronal differentiation of ESCs into cortical glutamatergic neurons was carried out as previously described.[117] In brief, the differentiation was carried out by adding doxycycline hyclate (2 μg/mL) to N2 supplemented media (Thermo Fisher, 17502048) with patterning factors SB431542 (Tocris, 1614, 10 μM), XAV939 (Stemgent, 04-00046, 2 μM) and LDN-193189 (Stemgent, 04-0074, 100 nM), as described previously.[117–119] Puromycin selection was used (5μg/μL), from days 2 to 6 to remove non-transduced cells. At 4 days post induction, neuronal cells were resuspended into Neurobasal media (Gibco, 21103049) that was supplemented with B27 (Gibco, 17504044, 50X), doxycycline (2 μg/mL), brain-derived neurotrophic factor (BDNF), ciliary neurotrophic factor (CTNF), and glial cell-derived neurotrophic factor (GDNF) (R&D Systems 248-BD/CF, 257-33 NT/CF, and 212-GD/CF at 10 ng/mL each). From this point onwards the neurons were either co-cultured with murine glial cells that were derived from early postnatal (P1-P3) mouse brains as described previously[120] or were left to grow as monocultures (mouse strain https://www.jax.org/strain/100012; animal ethical committee approval by Harvard University: Animal Experimentation Protocol (AEP) # 93-15).

Immunohistochemistry and imaging of ESCs

We performed immunohistochemistry on ESC-derived oligodendrocytes at 1, 5, and 10 days after doxycycline-based *SOX10* induction. Briefly, cells were grown on a 6-well plate and fixed using 2% PFA and then permeabilized using Triton-X (cat.# T9284-1L), followed by multiple washes with 1x Dulbecco's PBS at each step. We used the following primary antibodies for our immunohistochemistry experiments: anti-*O4* (cat. #MAB1326), anti-*MBP* (cat. #AB9348), anti-*NeuN* (cat. #MAB377), and anti-*PAX6* (cat. #AB78545). The primary antibodies were diluted in a solution of 10% bovine serum albumin (BSA) in phosphate-buffered saline (PBS) supplemented with 1% Triton-X then added to the cells and allowed to incubate overnight at 4°C. Cells were then washed three times in PBS. Finally, the secondary antibodies were diluted in a solution of 10% BSA in PBS supplemented with 1% Triton-X then added to the cells and allowed to incubate for 1-2 hours at room temperature. After the secondary incubation, one to two drops of ProLong Glass AntiFade Mountant with NucBlue (cat.# P36981) was added into the wells and coverslips were added on top of each cell culture into wells for downstream imaging.

Imaging of immunohistochemical stains was performed on a Keyence BZ-800XE microscope with a Nikon Apo 20x objective. All images were acquired using the same light emission settings and all channels were set to the same LUTs before quantification. For quantification, we used CellProfiler's IdentifyPrimaryObjects and MeasureObjectIntensity function to segment cells based on their DAPI signal. Subsequently, the average fluorescence value (mean intensity value) was normalized per cell to the average fluorescence intensity of the DAPI signal. To determine the significance of an intensity difference, a linear mixed-effect model was used to calculate the significance of a change in normalized intensity value across days of differentiation, treating each slice image as a random effect. Significance values were determined via a likelihood ratio test against the null model not containing the day of differentiation.

Generation of single-cell suspension from ESC-derived H1 iOligodendrocytes

To generate single-cell experiments, briefly we used oligodendrocytes at terminal differentiation (past day 8 post-doxycycline induction of SOX10). We isolated cells using the passaging protocol as mentioned above and measured cell concentrations in our isolate using a hemocytometer.

Read processing and clustering of iOligodendrocyte and iExcitatory Neuron scRNA-seq experiments

Sequencing reads from iOligo experiments were demultiplexed and aligned to the hg38 reference using CellRanger with default setting using the command CellRanger mkfastq, followed by count generation using the command CellRanger count. Sequencing reads from iExN experiments were demultiplexed and aligned to the hg38 reference using DropSeqTools with default setting.

To analyze single-cell RNA-sequencing data from ESC-derived oligodendrocytes and neurons we first determined highly variable genes using LIGER. We further used non-negative matrix factorization (with k, number of factors, set to 20) to determine a low-dimension embedding followed by graph-based clustering using SLM. Marker genes were identified by a Wilcoxon rank-sum and cells were annotated based on known markers of mature cell types as identified from our biopsy dataset.

ELISA-based amyloid beta quantification

To quantitate amyloid beta peptide levels from cell culture, we used the MesoScale Discovery V-Plex Plus Aβ Peptide Panel 1 (6E10) ELISA kit (cat. #K15200G). Briefly, we extracted 1.5mL of conditioned media per well replicate from isolates of ESC-derived oligodendrocytes, neurons, and microglia. Isolates were stored at -80°C till the ELISA assay was run at which time they were brought up to 4°C before being spun down at 10,000rpm for 15 minutes. The MSD ELISA was run according to the manufacturer's guidelines. Absolute Aβ peptide abundances were quantified using the MSD Discovery Workbench Analysis Software.

QUANTIFICATION AND STATISTICAL ANALYSIS

All statistical tests were two-tailed and were conducted in the R programming environment (v.4.0.4). A linear regression method was used to test the association between Biopsy Aβ burden and CSF Aβ42 levels. A Student's t-test was used to compare levels of phosphorylated tau and ELISA results between different groups of individuals. A logistic mixed-effect model with sex as covariate and subject as random effect to assess the changes in cell type proportion in response to AD pathology and test the association between changes in proportional changes in one cell type with differentially expressed genes in others. A Fisher's exact test was used to test for cell type proportional changes in the mouse microgla datasets due to experimental characteristics of these studies. The Benjamini-Hochberg procedure was used to correct for multiple testing. The Limma Trend approach, a linear mixed model with robust moderated t-statistics, was used to identify differentially expressed genes from log(count-per-milion + 1) normalized data from pseudocells with sex, cell type, $\log_2$(pseudocell MT%) and $\log_2$(pseudocell nUMI) as covariates and the subjects as random effects (using duplicateCorrelation() function from Limma). Pseudocells were constructed by aggregating the raw UMI counts of, on average, every 30 cells from the same cell type and individual. We excluded genes expressed in less than one percent of cell types from differential expression and GSEA analyses. For each cell type, subject-level logFC for Aβ+ and Aβ+Tau+ samples were calculated by applying the Limma Trend method to compare the expression across pseudocells from each subject to those from individuals without AD histopathology. Within each dataset, cell type markers were identified through a Wilcoxon rank sum test using the FindMarkers() function from Seurat. The robustness of identified differentially expressed genes was examined using a jackknife resampling procedure. Differential expression patterns between Aβ+ and Aβ+Tau+ groups were compared using a paired t-test. GSEA analysis was performed on protein-coding genes using the fGSEA package from Bioconductor that employs an adaptive multi-level split Monte-Carlo scheme to estimate the significance of patterns in gene sets. Meta analyses were performed using Stouffer's method where Z scores were calculated from test statistic p values. The significance of overlaps between two gene sets was tested using a Fisher's exact test. No statistical tests were used to predetermine sample sizes. No randomization was performed in our cohort assignment. Data analysis was not performed blind to the conditions of the experiments.

CellPress

Supplemental figures

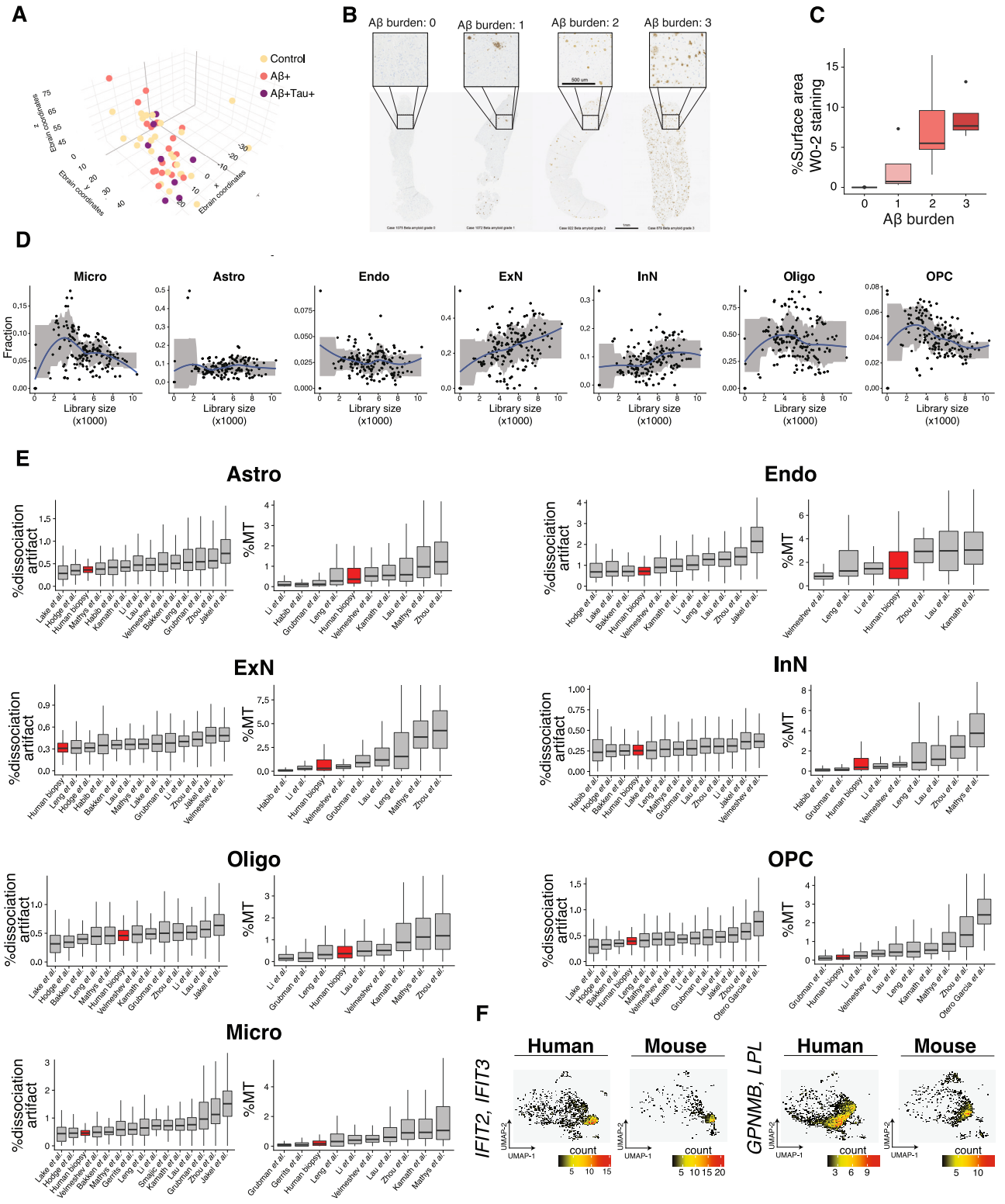

(legend on next page)

Figure S1. Stereological positioning and neuropathological scoring of biopsy cohort samples, related to Figure 1

(A) Relative three-dimensional coordinates of biopsy positions based on the mapping of post-surgical CT or MRI images from 52 subjects. Samples are colored by AD pathologic status.

(B) Representative images of biopsies with different Aβ burden.

(C) Comparison of Aβ burden based on our semi-quantitative microscopy-based approach with a quantitative method based on the percentage area coverage of W0-2 staining for a biopsy cohort of 24 individuals.

(D) Assessing the effect of the number of sequenced cells on the fraction of each cell class. The biopsy samples from the 52 individuals were sequenced in 173 libraries. Each dot represents the fraction of identified cells from the corresponding cell class in one library.

(E) QC metrics of human datasets parsed by major cell class. %MT, percent expression of genes per cell that map to mitochondrial genes, normalized by nUMI. % dissociation artifact, percent expression of dissociation-related artifactual genes[20] per cell and normalized by nUMI.

(F) Comparisons of some key microglia states between human and mouse datasets. Color indicates the number of human or mouse donors that support the expression of the gene in a given UMAP coordinate across datasets. See also Table S2.

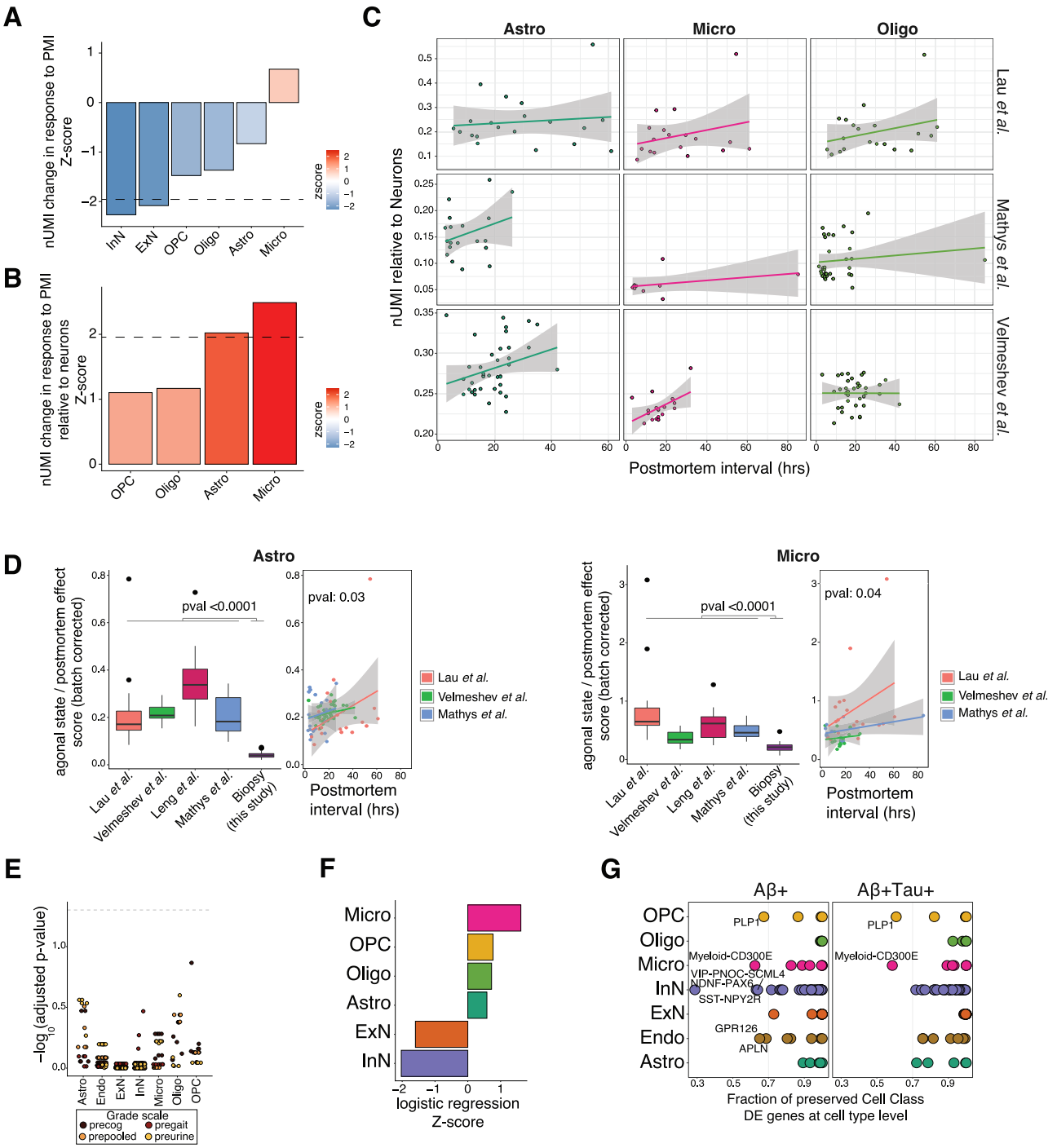

Figure S2. Peri- and postmortem effects on gene expression patterns, related to Figures 1 and 2

(A) Impact of postmortem interval on the number of expressed transcripts (nUMI) per cell class. To assess significance within each postmortem dataset, a regression line was fit to estimate the significance of association between postmortem interval (PMI) and the mean nUMI in each subject. For this analysis, we considered three postmortem datasets of Lau et al., Mathys et al., and Velmeshev et al. that their postmortem interval information were available and had sufficient range for a regression analysis. The p values from each dataset were next combined using Stouffer's method. To calculate the nUMIs per cell, we excluded the top 50 expressed genes in each dataset to better capture the impact of the postmortem intervals on the expression of the lower expressed genes. The dashed line represents the p value cutoff threshold of 0.05.

(B) Impact of PMI on glial-to-neuronal gene expression ratio. Within each of three postmortem datasets, similar to (A), a regression line was fit to examine the impact of the PMI on the mean ratio of glial-to-neuronal genes in each subject. The p values were next combined using Stouffer's method. In each subject, the

(legend continued on next page)

mean neuronal expression was calculated as the mean nUMI of excitatory and inhibitory neurons, excluding the top 50 expressed genes. The dashed line represents the p value cutoff threshold of 0.05.

(C) Glial-to-neuronal gene expression ratio as a function of PMI in each of the three postmortem datasets.

(D) Comparison of glial-to-neuronal gene expression levels between the biopsy and four postmortem datasets. Glial expression in each dataset was normalized to reduce the effect of the ambient RNA as measured by the expression level of the top 250 most specific markers of excitatory and inhibitory neurons. The neuronal specific gene markers were identified based on the pct.1 − pct.2 difference in our biopsy dataset. As shown, this normalization resulted in overlay of agonal state/postmortem scores for samples with a similar PMI across datasets.

(E) Dot plot of $-\log_{10}$-transformed FDR-adjusted p values from logistic mixed-effect model testing association of cell-type abundance with iNPH grading scale (GS) (STAR Methods) subscore severity measured prior to shunt placement (precog, cognitive subscale; pregait, gait subscale; preurine, urine subscale; pre-pooled, combined iNPH GS score).

(F) *Z* score from meta-analysis of major cell class level differential abundance comparing late-stage samples (Braak V and VI and Aβ+Tau+) versus pathology-free samples (STAR Methods).

(G) Cell class level differentially expressed genes are preserved within cell types. Cell types are labeled in which less than 70% of cell class level DE genes were preserved.

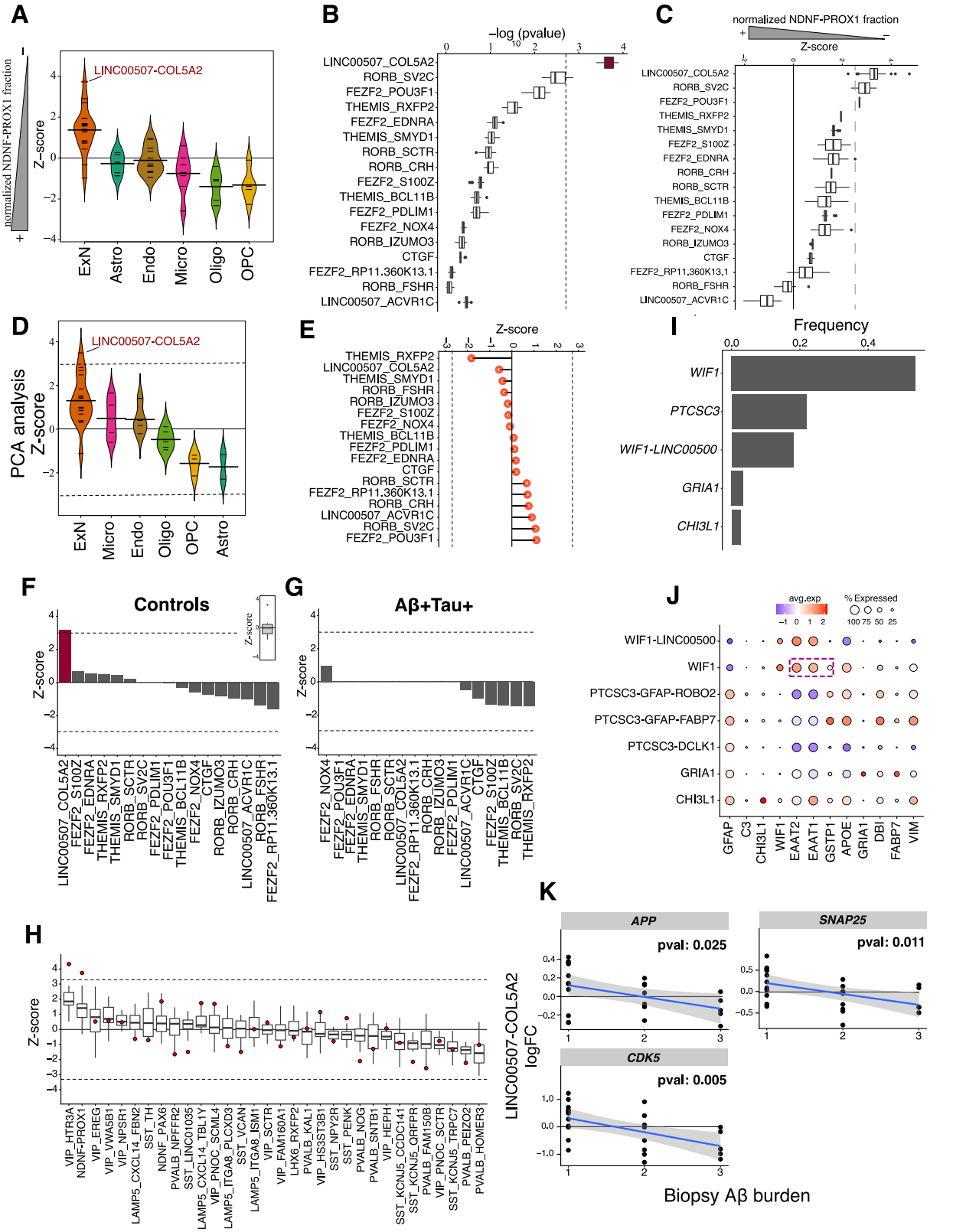

(legend on next page)

Figure S3. Loss of NDNF-PROX1 inhibitory neurons is associated with an upregulation of excitatory neuron DE signature, related to Figure 3

(A) Distribution of *Z* scores per cell class for the analysis shown in Figure 3A. Each small line indicates one cell type and the tick lines represent the mean.

(B) Logistic mixed-effect model regression (STAR Methods) of NDNF-PROX1 proportion versus ExN cell-type transcriptional signature in Aβ+ subjects with added poisson noise. Poisson noise counts were added to the UMI counts of each gene in each cell prior to computing the regression. Boxplots show the distribution of $-\log_{10}$ transformed p values over 30 noise iterations. Center line, median; box limits, upper and lower quartiles; whiskers, 1.5× interquartile range; points, outliers.

(C) Logistic mixed-effect model regression of NDNF-PROX1 proportion versus ExN cell-type transcriptional signature in Aβ+ subjects with downsampling of cells. Iterating 30 times, we randomly downsampled each ExN type to 7,000 cells, unless the cell-type size was less than this number. Boxplots show the *Z* score distributions over the 30 downsampling iterations. The dashed line indicates the FDR threshold of 0.05. Center line, median; box limits, upper and lower quartiles; whiskers, 1.5× interquartile range; points, outliers.

(D) Association between NDNF-PROX1 loss and LINC00507-COL5A2 cell type assessed using an alternative strategy of constructing a meta gene of the ExN DE signature from the first principal component (STAR Methods). Each small line indicates one cell type and the tick lines represent the mean.

(E) Logistic mixed-effect model regression of NDNF-PROX1 proportion versus ExN cell-type transcriptional signature in Aβ+ subjects after randomizing assignment of cells to excitatory cell types. Dashed line represents FDR threshold of 0.05.

(F and G) Logistic mixed-effect model regression (STAR Methods) of NDNF-PROX1 proportion versus ExN cell-type transcriptional signature in control (F) and Aβ+Tau+ (G) subjects. The inset boxplot in (F) shows the overall distribution of *Z* scores among the 17 excitatory neuron types. Dashed line represents FDR threshold of 0.05.

(H) Boxplots representing the association (as measured by *Z* score from logistic mixed-effect model regression) between each inhibitory neuron cell type (x axis) with the ExN DE signature across 17 ExN types (boxplots). The red dot represents the *Z* score of the LINC00507-COL5A2 type. Analysis is based on Aβ+ individuals only. In boxplots, center line, median; box limits, upper and lower quartiles; whiskers, 1.5× interquartile range.

(I) Barplots representing the relative frequencies of the five astrocyte cell types.

(J) Dot plots showing expression of astrocyte marker genes in each astrocytic cell type.

(K) LogFC expression of *APP*, *CDK5*, and *SNAP25* genes in LINC00507-COL5A2 excitatory neurons across increasing Aβ burden scores. Each dot represents the logFC in a sample with Aβ pathology versus control samples. Regression line is illustrated in blue with associated standard error.

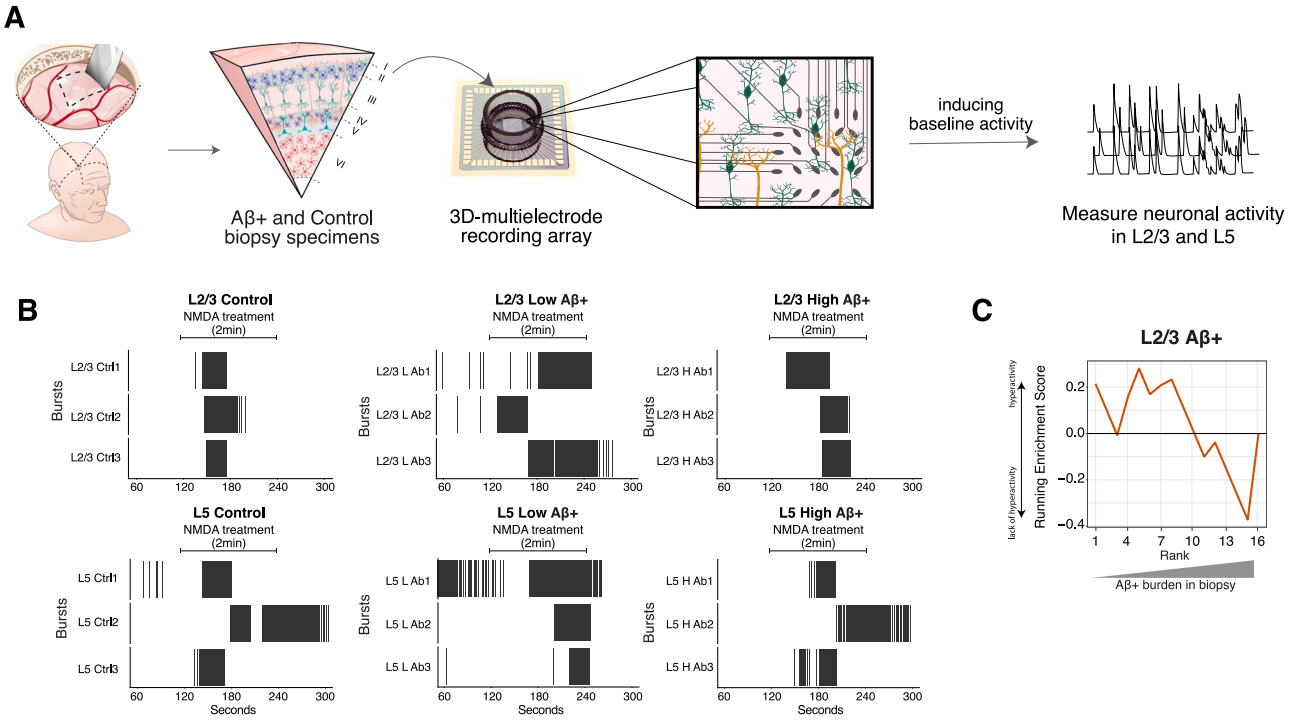

Figure S4. Hyperactivity of L2/3 excitatory neurons in biopsy samples with low burden of Aβ plaques, related to Figure 3

(A) Schematic representation of electrophysiology experimental design. Biopsy specimens were collected from an independent cohort of 26 individuals with varying degrees of Aβ pathology. Acute slices from the biopsies were then overlaid on 3D-multielectrode arrays and neuronal activity was measured after induction of activity by NMDA treatment.

(B) Representation of spike burst activity of top three electrodes from L2/3 (top) and L5 (bottom) neurons of three individuals from control, low Aβ, and high Aβ groups.

(C) Enrichment analysis of the 16 Aβ+ biopsies where samples are ordered based on their quantified burden of Aβ plaques. As illustrated, the trace analysis indicates samples with low Aβ+ burden are enriched for hyperactive L2/3 pyramidal neurons, consistent with Figure 3K (p value < 0.03). A hyperactivity *Z* score was calculated for each biopsy sample by comparing their adjusted number of bursts per second to the corresponding distribution in control samples. Aβ+ samples with *Z* score > 1.96 (p value < 0.025; one-sided) were marked as hyperactive. Number of bursts per seconds were adjusted across all samples by regressing out the effect of age using a linear model. We observed similar patterns without this adjustment (data not shown).

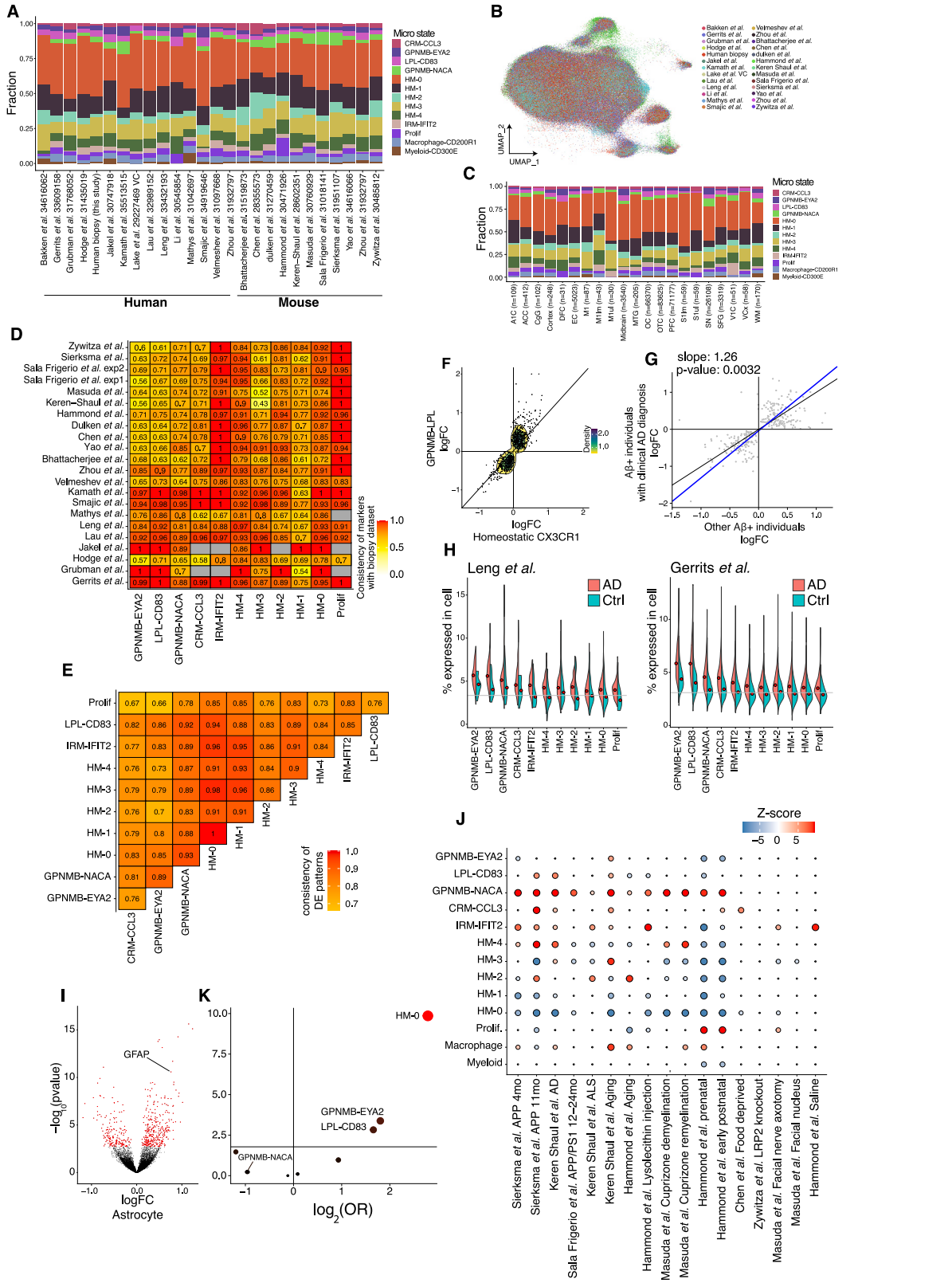

(legend on next page)

Figure S5. Microglia responses to the accumulation of Aβ and tau in cortical tissue, related to Figure 4

(A) Microglia cell state compositions across human and mouse datasets.

(B) UMAP representation of microglia integrative analysis where each cell is colored by its dataset of origin.

(C) Proportion of microglial states stratified by brain region.

(D) Marker expression consistency of previous human and mouse single-cell datasets with the biopsy dataset. Consistency score is defined as the fraction of markers from human biopsy dataset for each microglia state that show a conserved up- or downregulation pattern in each dataset.

(E) The fraction of DE genes from the biopsy dataset between each pair of microglia states that have a conserved logFC pattern (e.g., up or down in both cell states). DE genes were calculated by comparing Aβ+/Aβ+Tau+ samples with controls.

(F) Comparison of DE genes between GPNMB-LPL and CX3CR1 microglia types in the biopsy dataset. The analysis is based on the union of top 300 DE genes in each cell type to reduce the impact of cell-type size variation (i.e., statistical power).

(G) Comparison of DE genes in microglia between the 9 Aβ+ individuals that are clinically diagnosed with AD within 5 years from the biopsy collection and the remaining 10 Aβ+ individuals.

(H) Microglia DE genes from the biopsy dataset are upregulated in two AD postmortem studies and are enriched for the markers of GPNMB-LPL and LPL-CD83 microglia states. Meta-gene expression of the upregulated microglial DE genes from our dataset in two published postmortem studies.[4,6] The meta-gene was constructed by summing their UMI counts in each cell and normalizing by the nUMI. The gray lines illustrate the median expression of the meta-gene across microglia states.

(I) Differential expression analysis of astrocyte genes in response to Microglia GPNMB-EYA2 and LPL-CD83 expansion. The DE genes (FDR-adjusted p value < 0.05) are represented in red. Fractions of microglia GPNMB-EYA2 and LPL-CD83 cells in individuals are normalized using an empirical normal cumulative estimation function (ecdf function in R) to have a range between zero and one.

(J) Enrichment of mouse microglia states in response to various conditions (Fisher's exact test; FDR-adjusted p value < 0.1).

(K) Overlap between top 100 microglia state markers and the genes in proximity with human-accelerated regions (HARs).[47]

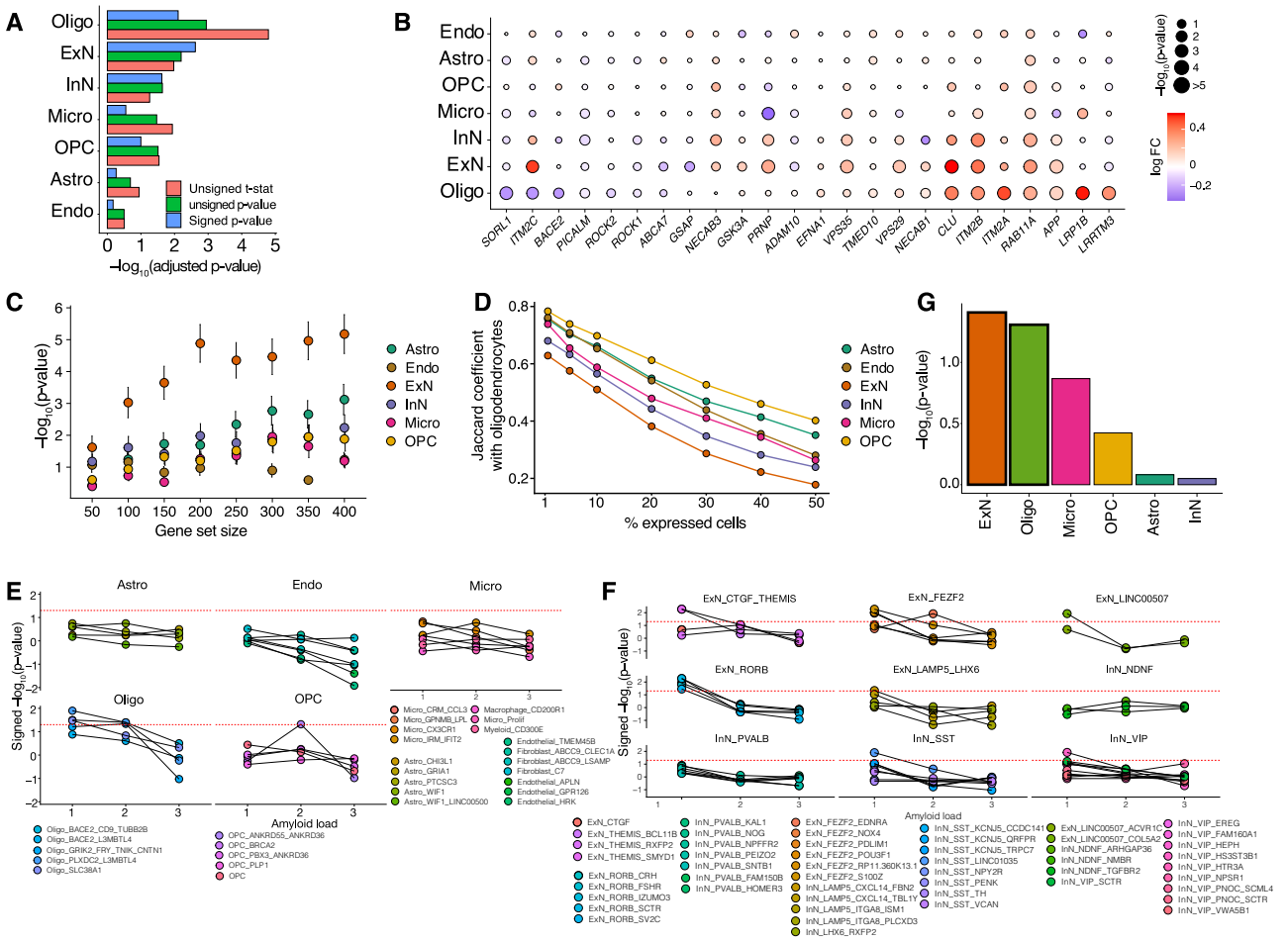

Figure S6. Nomination of amyloid-producing cell types in the human frontal cortex, related to Figure 5

(A) Bar chart showing $-\log_{10}$-transformed p values for various ordering statistics (indicated at bottom right) based on GSEA of Aβ production and secretion geneset (Table S5) and cell class DE genes.

(B) Dot plot denoting differential expression of leading-edge genes, identified by the GSEA of Aβ gene set in Figure 5A, in Aβ+ subjects versus Aβ-free biopsy samples. Color correlates with logFC and size correlates to $-\log_{10}$-transformed p values.

(C) Correlation analysis results obtained via fast gene set enrichment analysis (fGSEA) (see STAR Methods) comparing differentially expressed gene lists between all major cell classes and oligodendrocytes, with increasingly liberal thresholds (larger gene lists) for assigning univariate significance.

(D) Overlap of genes expressed in oligodendrocytes with other major cell classes. Different thresholds were selected to consider a gene as expressed (x axis) based on the percentage of the cells in which the gene has non-zero UMI.

(E and F) Signed $-\log_{10}$-transformed p values associated with fGSEA enrichment across increasing Aβ and tau burdens for all major cell types (glia in E and neurons in F) in human frontal cortex from DE analysis of the human biopsy dataset.

(G) Meta-analysis p values for GSEA of the Aβ associated gene set in the DE genes of two postmortem AD case-control datasets,[3,4] for six cell classes. Bolded bars indicate FDR significance.

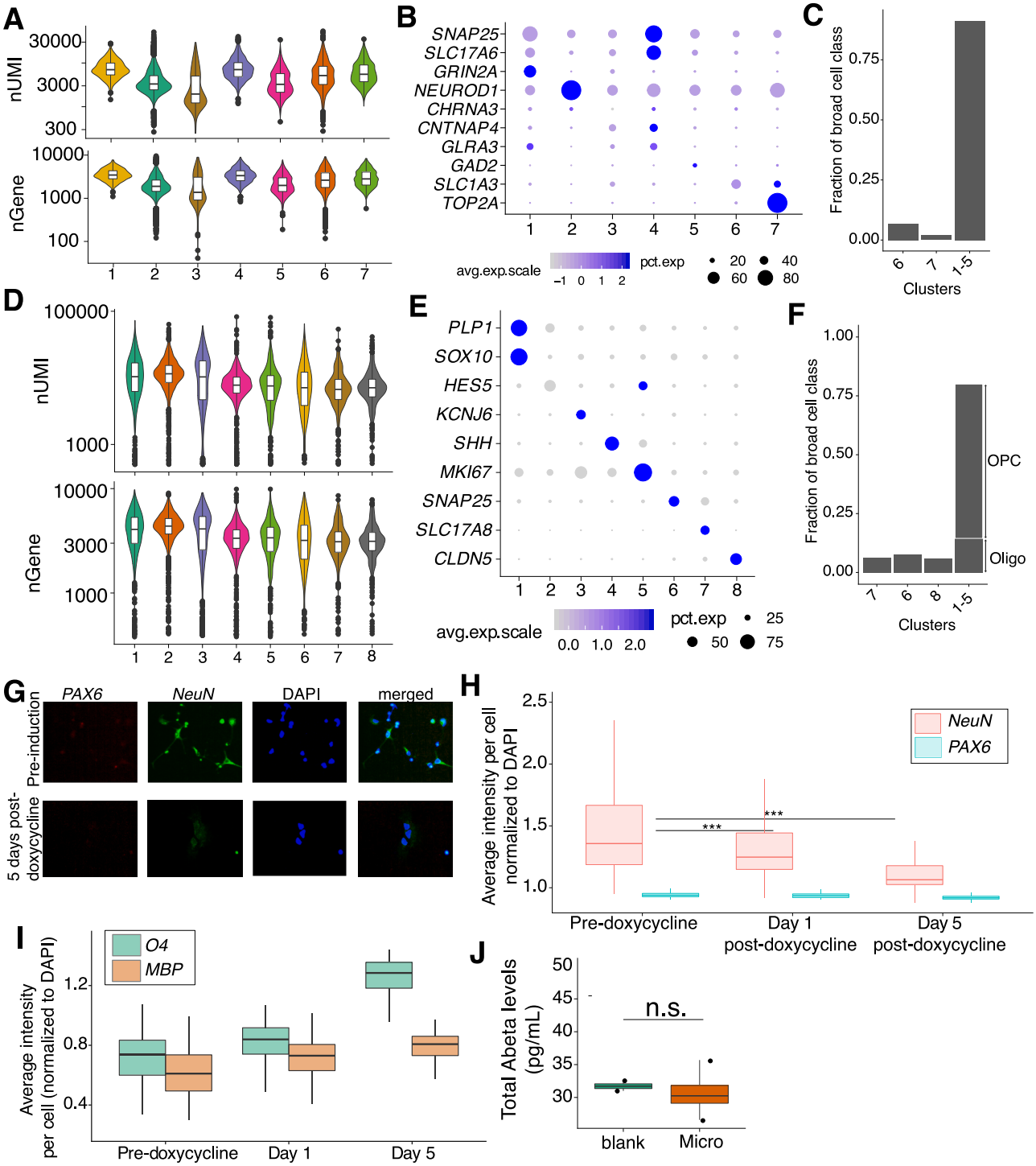

Figure S7. Single-cell transcriptomics and immunohistochemistry of ESC-derived oligodendrocyte and neuron cultures, related to Figure 6

(A and D) Violin plot of number of nUMI (top) and nGene (bottom) per cell type identified in single-cell transcriptomics of ESC-derived neuron (A) and (D) oligodendrocyte lineage cultures. In boxplots, center line, median; box limits, upper and lower quartiles; whiskers, 1.5× interquartile range; points, outliers.

(B and E) Key marker genes for cell types identified from single-cell transcriptomics of ESC-derived iExN (B) and (E) iOligo cultures.

(C and F) Composition of ESC-derived iExN (C) and iOligo (F) cultures based upon single-cell cluster annotations.

(G) Representative images of immunofluorescence stains of *PAX6* and *NeuN* (G) in ESC-derived iOligo cultures.

(legend continued on next page)

(H and I) Boxplots of average intensity values per cell (normalized to DAPI intensity) across days of differentiation for *NeuN*, *PAX6* (H), *O4*, and *MBP* (I). Box upper and lower bounds represent upper and lower quartiles and Whisker distance from upper and lower hinges represents $\leq$1.5 times the interquartile range. Center line indicates the median value.

(J) Total Aβ levels from conditioned media isolated from ESC-derived microglia and blank control derived from unconditioned oligodendrocyte differentiation media. *** $p < 0.001$, ** $p < 0.01$, * $p < 0.05$, n.s., not significant. Statistical tests are based on a linear mixed-effect model that compares immunofluorescence signal intensity per cell using each sample well as the levels of the random effect. Statistical significance for comparing β-amyloid protein values was determined via the Student's t test.